Università degli Studi di Pavia

Faculty of Engineering
Department of Electrical, Computer and Biomedical Engineering

Master Degree in Industrial Automation Engineering
Robotics and Mechatronics

Development and Validation of an Optical Measurement System for Tool Presetting

Supervisor:
Luca Lombardi

Co-supervisor:
Alessandro Peverelli

Candidate:
Lorenzo Cabri

Student ID:
549158

Academic Year 2024/2025

Abstract

In today's manufacturing landscape, rigorous verification of cutting tool geometry is essential to ensure efficiency and tight tolerances in CNC machining. Currently, industrial presetting systems rely mostly on two-dimensional optical vision technologies which, despite being able to extract macro-geometries such as maximum diameters, are unable to detect volumetric parameters crucial to cutting performance, such as the rake angle and the clearance angle.

This thesis proposes the development and integration of an automated 3D measurement system to overcome these limitations. Following a comparative analysis of optical technologies, laser triangulation was selected as the optimal architecture to balance micrometre-level accuracy, measurement field of view and scanning speed. The sensor was initially subjected to rigorous laboratory validation to test its performance, stability and repeatability on highly reflective metal surfaces, characteristics typical of cutting edges.

The device was subsequently physically integrated into a Speroni presetting machine. To enable automated data extraction independent of the operator, a processing algorithm based on Iterative Robust Fitting was developed. Starting from a user-defined Region of Interest (ROI), the algorithm autonomously filters out optical noise and geometric irregularities, iteratively discarding outliers based on a definable threshold, until it converges robustly on the actual cutting edge segment

Experimental tests conducted on industrial samples have confirmed the system's excellent reliability, achieving accurate measurements with standard deviations close to zero. In addition to eliminating operator dependency, the algorithm successfully identified a manufacturing geometric anomaly in one of the analysed parts, demonstrating the system's effectiveness as an advanced diagnostic tool for quality control and 3D presetting.

Sommario

Nel moderno panorama manifatturiero, la verifica rigorosa della geometria degli utensili da taglio è essenziale per garantire efficienza e tolleranze ristrette nelle lavorazioni CNC. Attualmente, i sistemi di presetting industriale si basano prevalentemente su tecnologie di visione ottica bidimensionale che, nonostante siano in grado di estrarre macro-geometrie come i diametri massimi, sono incapaci di rilevare parametri volumetrici cruciali per le prestazioni di taglio, come l'angolo di spoglia e l'angolo di petto.

Questa tesi propone lo sviluppo e l'integrazione di un sistema di misurazione 3D automatizzato per superare tali limitazioni. A seguito di un'analisi comparativa delle tecnologie ottiche, la triangolazione laser è stata selezionata come l'architettura ottimale per bilanciare precisione micrometrica, ampiezza del campo di misura e velocità di scansione. Il sensore è stato inizialmente sottoposto a una rigorosa validazione di laboratorio per testarne le performance, la stabilità e la ripetibilità su superfici metalliche altamente riflettenti, caratteristiche tipiche dei taglienti.

Successivamente, il dispositivo è stato integrato fisicamente su una macchina di presetting Speroni. Per permettere un'estrazione dei dati automatizzata e indipendente dall'operatore, è stato sviluppato un algoritmo di elaborazione basato su Iterative Robust Fitting. Partendo da una Region of Interest (ROI) definita dall'utente, l'algoritmo filtra autonomamente il rumore ottico e le irregolarità geometriche, scartando iterativamente gli outlier in base a una soglia definibile, fino a convergere in modo robusto sul reale segmento del tagliente

I test sperimentali condotti su campioni industriali hanno confermato l'ottima affidabilità del sistema, restituendo misurazioni accurate con deviazioni standard prossime allo zero. Oltre a eliminare la dipendenza dall'operatore, l'algoritmo ha permesso di identificare con successo un'anomalia geometrica di fabbricazione in uno dei pezzi analizzati, dimostrando l'efficacia del sistema come strumento diagnostico avanzato per il controllo qualità e il presetting 3D.

Contents

List of Figures

List of Tables

List of Acronyms

CNC Computer Numerical Control

BUE Built-up Edge

CMOS Complementary Metal-Oxide-Semiconductor

VDI/VDE Verein Deutscher Ingenieure / Verband der Elektrotechnik

ROI Region of Interest

FOV Field of View

MR Measurement Range

CD Clearance Distance

Chapter 1

Introduction

In modern manufacturing, Industry 4.0 has transformed production methods by introducing high levels of automation and data integration, allowing today's CNC machines to operate at high speeds and extreme precision to meet the strict dimensional tolerances required by sectors like aerospace, automotive, and biomedical engineering. Since the cutting tool acts as the main physical interface between the machine and the workpiece in these advanced systems, any dimensional deviation transfers directly to the final product, making precise monitoring and preliminary characterization of its geometry essential to guarantee high machining standards.

During the machining process, cutting edges face severe mechanical stress, thermal fluctuations, and continuous friction, leading to a natural wear of the tool geometry. If this degradation is not carefully monitored, excessive wear or unpredictable microbreakages can compromise the surface finish of the machined part, and if not timely resolved, can lead to undetected tool failures that generate out of tolerance components, resulting in higher scrap rates, machine downtime, and significant economic losses. Therefore, checking the geometric integrity of cutting tools is a basic requirement to maintain the efficiency of any modern production line.

Historically, tool wear evaluation relied on subjective visual inspections by the operator or required sending the tools to a temperature-controlled metrology room. While a specialized laboratory offers excellent accuracy, this workflow is very time-consuming and creates a production bottleneck; on the other hand, manual visual inspections are prone to errors and fail to provide the certified traceability required to meet modern metrological quality standards. To solve this

issue, the industry has widely adopted tool presetting and measuring machines, which can be installed directly on the shop floor next to the CNC machines, allowing operators to measure the tool geometry offline while the main machine is working, reducing setup time and ensuring that only validated tools are loaded into the spindle. However, standard presetting machines usually analyze the two-dimensional silhouette of the cutting edge using backlight illumination. While this is effective for extracting macro-geometric parameters like maximum diameter or overall length, a 2D optical projection cannot fully evaluate complex volumetric wear, cratering, or localized micro-chipping on the reflective cutting face. To achieve a complete and automatic wear analysis, the inspection system must move from a flat profile evaluation to a full 3D surface reconstruction.

To solve this technological gap, this thesis presents the development and practical implementation of a fully automated 3D scanning system integrated directly into a tool presetting machine. The research was carried out through an industrial collaboration with Speroni, a globally recognized manufacturer of advanced presetting machines, and iMAGE S, an engineering company specialized in machine vision and optical metrology.

The project workflow was divided into three main phases. First, with the technical support of iMAGE S, a theoretical analysis of available optical technologies was performed to find an architecture that satisfies specific measurement requirements and micrometer tolerances despite the reflection issues typical of metallic surfaces. After choosing laser triangulation, iMAGE S provided the optical sensor for a series of laboratory tests, a crucial validation phase focused on extracting the empirical data needed to verify the sensor performance under controlled conditions. Finally, the project addressed the engineering challenge of physical and software integration of the laser profiler onto the Speroni presetting machine, culminating in a fully functional automatic 3D wear inspection system capable of operating directly on the shop floor.

The thesis is organized as follows:

- **Chapter 2** gives an overview of the state of the art, analyzing the tool cutting edge angles that are prone to wear and how their geometry affects cutting performance. It also evaluates the current Speroni machines limitations and the competititors transition toward 3D measurement systems.

- **Chapter 3** reviews the 3D optical technologies considered for the Speroni machine, comparing their physical principles to find the best solution.

- **Chapter 4** describes the preliminary experimental phase, detailing the laboratory tests done with the laser sensor to check its performance and reliability on reflective metals.
- **Chapter 5** covers the physical and software integration of the measurement system into the Speroni machine, explaining how the automated inspection process was developed.
- **Chapter 6** concludes the thesis by analyzing the scanning results, followed by some closing thoughts and a discussion on future developments.

Chapter 2

State of the art

The efficiency of material removal processes is closely related to the quality and geometric precision of the cutting tools. In modern industry, which involves very tight tolerances and hard-to-machine materials, cutting edge geometry is not only a design parameter, but it is a critical factor determining tool life, surface finish, and the stability of the entire machining system. The most important parameters include the rake angle (γ) and the clearance angle (α), since their correct configuration is essential to optimize the formation of the chip and reduce the cutting forces. Measuring these angles presents a fundamental challenge, as they are not simple linear dimensions but rather define the spatial orientation of tiny surfaces with complex helical profiles.

Currently, the standard approach used by Speroni S.p.A. relies on telecentric optics and advanced edge detection algorithms to analyze the 2D projected tool silhouette, to accurately capture absolute profile measurements such as maximum diameters and overall lengths. However, this method presents a major physical limit: by analyzing a side projection of the tool, the system cannot obtain depth information along the optical axis, so the true spatial inclination of the rake and clearance faces cannot be measured using only a two-dimensional edge analysis.

This chapter begins by analyzing specific tool cutting edge angles and how they affect cutting performance and surface finish, making their precise measurement a fundamental requirement for high-quality machining. Next, it evaluates current Speroni S.p.A. systems to identify the physical constraints that prevent traditional 2D imaging from capturing these spatial angles, and then it looks at the market to see how competitors have solved these measurement problems by moving to 3D system solutions.

2.1 Tool Geometry

Understanding a cutting tool's performance requires a closely look its micro-geometry, since the position of the cutting edges determines the efficiency of material removal. The spatial orientation of the two primary surfaces forming the cutting edge plays a crucial role in this dynamic: the rake face (the upper surface along which the chip flows) and the flank face (the back surface facing the newly machined workpiece).

The angle between these surfaces is not a random design choice, but it represents a careful balance between maximizing the mechanical strength of the cutting edge and ensuring efficient chip evacuation. Therefore, accurate measurement of the rake angle (γ) and the clearance angle (α) is essential to control the thermomechanical interactions between the tool and the workpiece.

2.1.1 Rake angle

The rake angle, denoted by the symbol γ, is a key geometric parameter that determines the behavior of the tool during machining operations. It is the angle the angle between a reference plane perpendicular to the cutting direction and the rake face, which is the main contact area where the material is deformed and removed to form the chip. Therefore, the size of this angle determines the cutting mechanics: it decides how much of the machine's power is used for material removal instead of being lost as heat or vibrations [1].

Depending on the orientation of the rake face, the rake angle can be positive, negative, or neutral (zero). Each configuration changes how the chip is formed, creating a trade-off between the mechanical strength of the cutting edge and the energy efficiency of the machining process.

A positive rake angle ($\gamma > 0$) is used to increase cutting efficiency. In this configuration, the tool has a sharper profile that wedges under the material, increasing the shear angle and reducing the plastic deformation zone. Increasing the positive rake angle can reduce the tangential cutting force by 10% to 25%, providing a significant advantage when machining ductile materials like aluminum alloys or low-carbon steels. This reduced mechanical stress provides several benefits:

- **Lower heat:** Less cutting resistance means less friction and heat at the tool-chip interface, protecting the edge and improving the surface finish.
- **Better chip flow:** A positive angle helps chips evacuation, preventing the formation of a built-up edge (BUE).

A BUE occurs when layers of the workpiece weld to the tool under pressure [2], which is a common issue with stainless steels or high-temperature materials. As the built-up material accumulates and is subsequently torn away during cutting, it gradually damages the original micro-geometry, eventually leading to brittle fracture and premature edge failure. However, optimizing for maximum cutting efficiency requires a structural compromise. A highly positive angle significantly reduces the volume of tool material supporting the cutting edge; as a result, the tool tip becomes much more susceptible to fracture under heavy impacts, and this reduced mass diminishes the tool's capacity to dissipate heat, accelerating wear when machining very hard or abrasive materials.

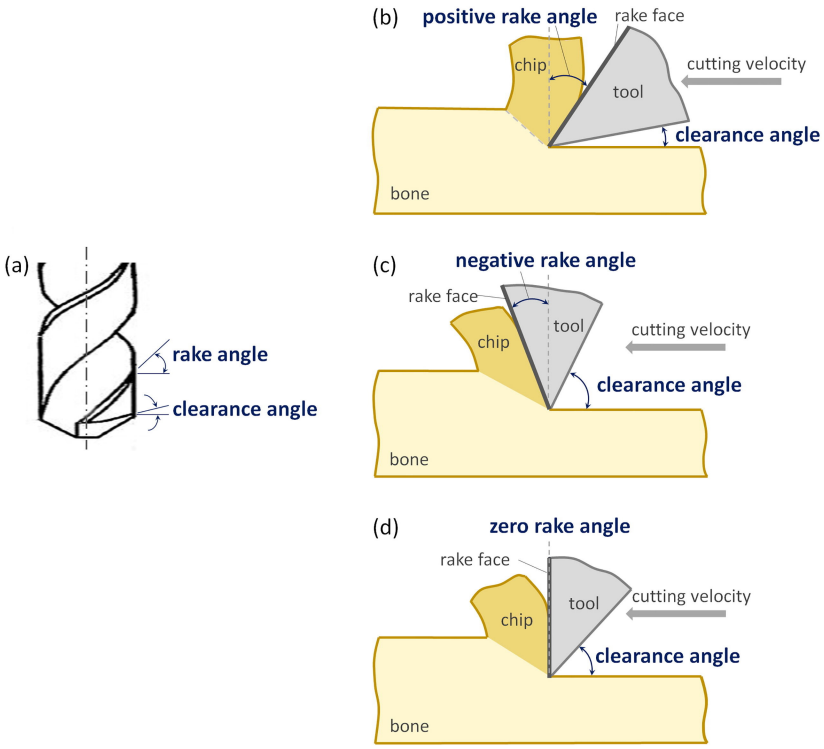

Figure 2.1: Schematic representation of positive, negative, and neutral rake angle configurations [3].

In contrast, a negative rake angle ($\gamma < 0$) is used to change the stress distribution. In this configuration, the rake face tilts away from the cutting direction, applying a strong compressive force on the material rather than shearing it. While this requires more power and a more rigid machine, it offers much higher mechanical strength:

- **Edge protection:** By shifting the load away from the tip, the negative angle protects the most fragile part of the tool.

- **Durability:** By maximizing edge strength, this geometry can withstand the constant impacts of interrupted operations like milling and the heavy roughing of high-strength materials, preventing the fractures that would easily destroy a sharper tool.

- **Heat dissipation:** The larger volume of tool material helps absorb and spread heat, allowing the tool to handle high feed rates and temperatures without losing its hardness.

Finally, a neutral or zero rake angle ($\gamma = 0$) is suited for applications where process stability is more important than pure cutting efficiency. Commonly used for brittle or short-chipping materials like cast iron, brass, or specific bronzes, a neutral rake angle prevents the tool from unpredictably over-engaging with the workpiece. This self-feeding effect is a risk with highly positive geometries, as it can cause chatter vibrations or cause the cutting edge dig in. As a result, a neutral geometry offers an good compromise between easier tool resharpening and maintaining a constant depth of cut, ensuring a stable machining operation.

The strong correlation between the rake face geometry and the tool's thermo-mechanical response makes this angle a critical parameter for process stability. Using a cutting tool whose actual rake angle deviates from its nominal value leads to highly unpredictable machining outcomes, where the difference of cutting forces and temperatures from theoretical models triggers premature wear or chatter vibrations that severely degrade the workpiece's surface integrity. Accurately measuring the spatial orientation of this surface is essential to ensure that cutting energy is used efficiently for chip formation, rather than lost as heat or internal stresses that could fracture the cutting edge. Therefore, implementing a technology capable of strictly verifying this angle's value becomes a fundamental step, elevating advanced optical metrology from mere quality assurance to a vital link between theoretical design and real-world performance.

2.1.2 Clearance angle

The clearance angle, denoted by the symbol α, is defined as the angle of the flank face relative to the tangent of the newly cut surface. While the rake angle governs chip formation, the clearance angle is essential to prevent the tool from rubbing against the workpiece. Without it, the tool's flank would drag against the machined material, generating excessive friction and heat rather than facilitating a clean cut [4].

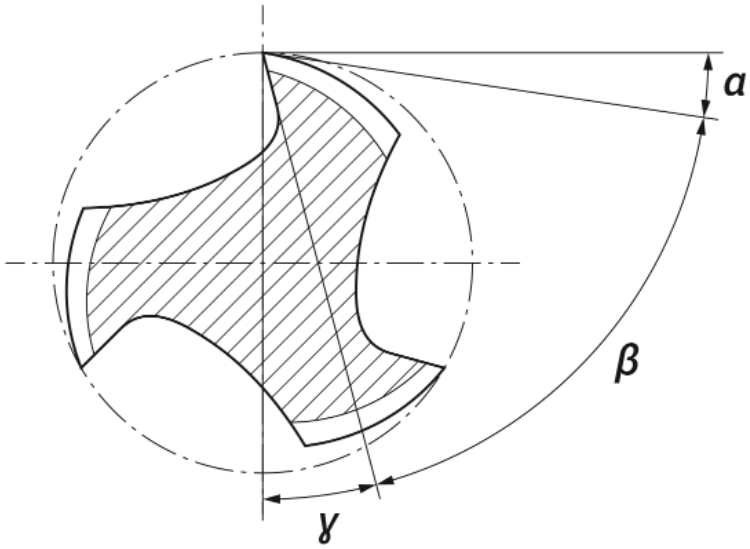

Figure 2.2: Relationship between clearance (α), wedge (β), and rake (γ) angles.

Designing this angle requires a trade-off: a smaller clearance angle results in a larger cross-section for the cutting edge, providing better mechanical support which is essential for machining high-strength or hardened materials, where elevated cutting forces could easily fracture a thinner profile. However, an excessively small clearance angle fails to provide adequate space for the material's elastic recovery, which is a fundamental concept in metal cutting theory [5]. Since the newly cut surface expands slightly due to elastic springback immediately after shearing, an insufficient clearance angle forces the tool flank to rub against the material; this continuous frictional contact not only accelerates flank wear and degrades the surface finish, but also generates intense localized heat that can alter the part's metallurgical structure, causing harmful residual stresses and unwanted work hardening.

On the other hand, a large clearance angle minimizes friction, allowing a more efficient cutting process, which is particularly advantageous when machining soft materials or light alloys that tend to tool adhesion. However, this free-cutting advantage compromises structural stability: excessive clearance thins the tool profile, making it much more prone to chatter vibrations and chipping under load. To solve this, modern cutting tools often use a dual-geometry design featuring a primary clearance immediately right next to the cutting edge and a secondary clearance further back, preventing rubbing while keeping the highly stressed tip mechanically strong.

Closely linked to these parameters is the wedge angle (β), which is the structural core of the cutting edge. Defined by the intersection of the rake and flank faces to dictate the thickness and mechanical robustness of the tool tip, this angle completes the fundamental geometric relationship linking the three primary parameters in the standard orthogonal cutting model seem in fig. 2.2:

$$\alpha + \beta + \gamma = 90^\circ$$

The size of the wedge angle (β) controls the trade-off between the sharpness of the cutting edge and its structural strength. A small wedge angle means a sharp profile that easily penetrates the material. However, this narrow geometry makes the tool tip fragile and reduces its ability to dissipate heat [6]. Conversely, a large wedge angle provides the mechanical mass needed to machining harder materials, offering better stability under heavy loads. However, an excessively large wedge angle restricts the space available for the rake and clearance angles, resulting in an overly thick tool that struggles to penetrate the workpiece, generating excessive friction and heat, which accelerates wear and increases the machine's power consumption.

The stability of the cutting process heavily relies on the precise balance of these angles at the cutting edge. If the rake or clearance angles deviate from their nominal values, the tool can easily switch from a smooth shearing action to rubbing, causing overheating that degrades the workpiece surface and shortens the tool's life. Similarly, the wedge angle acts as the main structural defense against mechanical failure, where any geometric deviation can make a tool either too fragile or highly inefficient. This strong link between the cutting angles shows why accurate 3D topographical mapping has become an industrial necessity. In modern industry, where manufacturing tolerances are very tight, relying on a standard 2D estimate of the tool profile is no longer enough; only precise 3D measurements of the actual face angles can guarantee peak operational efficiency and prevent the geometric errors responsible for machine downtime and material waste

2.2 Current Presetting Systems

As described in the previous section, accurately measuring both the rake and clearance angles is essential for optimal cutting tool performance. To understand the related measurement challenges, this analysis focuses on the STP FUTURA system by Speroni S.p.A. as a primary example of modern tool presetting technology. [7].

The STP FUTURA system is designed to provide a highly stable base, which is necessary for integrating high-resolution measurement instruments. It features a cast iron supporting structure to minimize thermally induced structural deformations, integrated with an advanced CNC system, where linear axis translation and precise spindle indexing ensure fluid motion and sub-micrometric positioning repeatability. As a result, this setup ensures that the optical scanning phase is not affected by any positioning errors or internal mechanical vibrations.

Figure 2.3: Speroni STP FUTURA tool presetting and measuring system.

Integrated with the mechanical structure, the optical acquisition process relies on two-dimensional vision technologies. In this configuration, the cutting edge inspection is performed using a backlighting technique, where a projector illuminates the tool from one side, and a sensor on the opposite side detects the light. The tool blocks the beam, appearing pitch-black against a bright background to generate a high-contrast video stream, which is processed in real time

by mathematical algorithms to accurately analyse the tool's geometry.

As shown in fig. 2.4, the measurement principle currently implemented on the Speroni system relies on advanced edge detection algorithms, which uses the sharp optical contrast between the backlit tool and the bright background to capture the projected profile of the cutting edge. Analyzing the sensor output shows that this 2D representation is fully capable of verifying external macroscopic features, like the helix angle or the maximum working diameter.

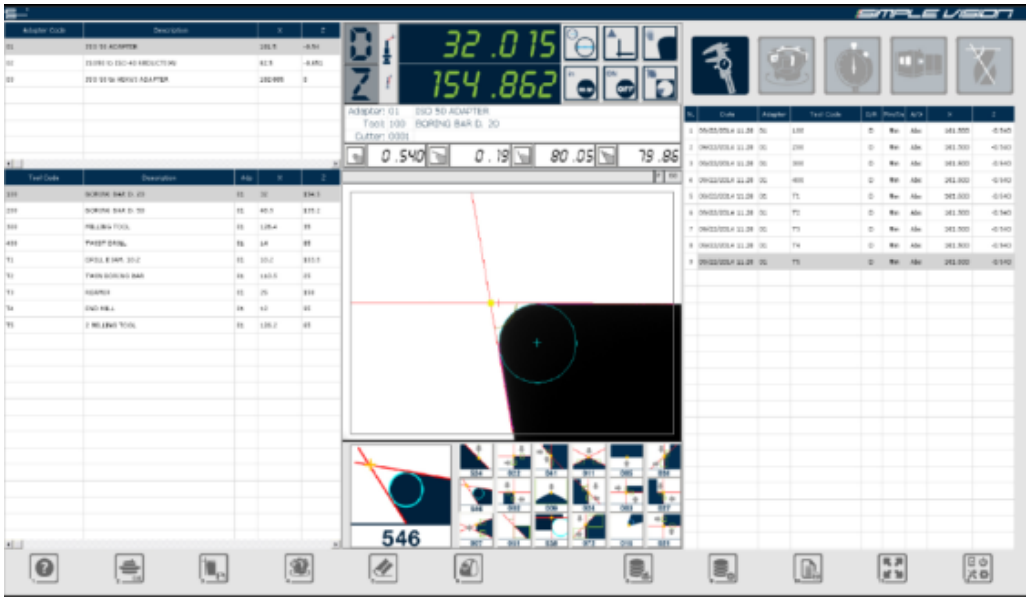

Figure 2.4: 2D optical edge detection of a backlit cutting tool profile.

However, in 2D analysis, all depth information is lost because the tool's volume is projected flat onto the camera sensor, and micro-geometric parameters likes the rake and clearance angles are hidden within the dark silhouette of the tool, making it impossible to measure these parameters using only the 2D perimeter.

To overcome the limits of 2D optical projection, it is useful to look at how the metrology market has solved the problem of hidden micro-geometry, where several manufacturers have bypassed the dark silhouette issue by integrating 3D scanning modules directly into their measurement systems.

A clear example is the system developed by Zoller. As documented in an industrial case study [8], Zoller solved the hidden geometry problem by collaborating with LMI Technologies, which is one of the leading company in optical sensors. During the development phase, the engineering teams evaluated several 3D scanning methods, focusing mainly on infinite focus and confocal microscopy. However, to meet industrial demands, they chose structured light fringe projection

(section 3.2).

By projecting multiple fringe patterns directly onto the tool faces, the scanner captures surface deformations to generate a full three-dimensional point cloud. This architecture enables the measurement of micro-geometric parameters, such as the exact inclination of the rake angle and the edge preparation rounding, achieving sub-micron accuracy and being able to overcome the limits of traditional 2D shadow analysis.

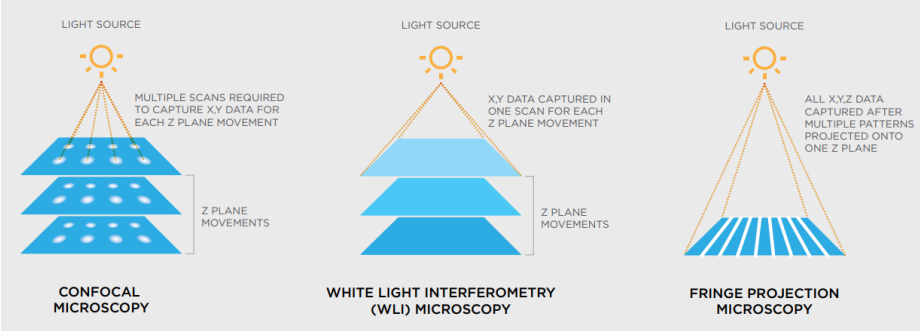

Figure 2.5: Comparison of advanced optical measurement principles evaluated for three-dimensional tool inspection.

Alongside structured light applications, a significant industrial alternative is offered by Bruker Alicona, whose technology uses focus variation (section 3.4) for the comprehensive inspection of cutting tools [9]. By employing optical 3D micro-coordinate measurement machines, these systems generate a complete digital reconstruction of the cutting wedge within a single automated setup [10]. While the underlying optical theory is analysed in the following section, its practical application already provides a level of volumetric detail that can't be obtained by traditional 2D imaging. Indeed, by rapidly scanning the tool surface across multiple focal planes, these systems combine a high depth of focus with high data density, which is a fundamental characteristic in precision manufacturing for the measurement of macroscopic geometry and sub-micrometer surface roughness. The resulting high-density 3D topographical maps offer true colour representation alongside high vertical resolution, allowing for the precise measurement of angular profiles while concurrently inspecting micro-geometric features like edge radius and micro-chipping.

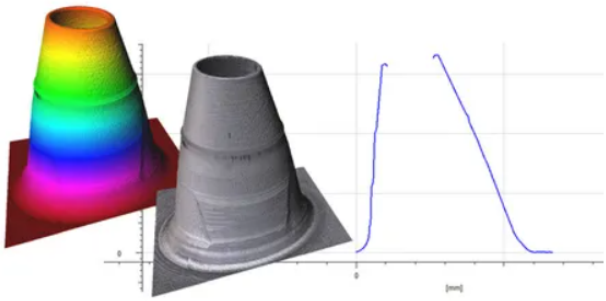

Figure 2.6: Three-dimensional topographical reconstruction of a cutting edge acquired through focus variation technology.

These industrial implementations show that accurately digitizing the entire cutting wedge is not only possible, but necessary to meet modern metrological standards. While the use of structured light projection and focus variation highlights a market shift toward volumetric analysis, the landscape of 3D scanning extends beyond these specific examples. The following section will analyse the fundamental physical and mathematical principles governing a wider spectrum of three-dimensional acquisition technologies currently available, alongside the previously discussed methods, providing the necessary scientific foundation to fully evaluate their respective metrological capabilities, and identify which one is most suitable approach for our project.

Chapter 3

3D Acquisition Technologies

After identifying the limits of 2D projection and the market trends in chapter 2, upgrading to 3D measurement systems becomes necessary to overcome the metrological uncertainty of 2D vision. Measuring both the maximum profile and the actual topography of the cutting edge requires technologies capable of capturing depth data. To solve this industrial requirement, this chapter explores the main non-contact 3D scanning methodologies applicable to tool metrology. The objective is to evaluate their physical operating principles, potential, and limits: by comparing these methods with the strict precision requirements and the challenges of highly reflective metals, this analysis justifies the final technological selection for the next generation Speroni machines, aiming for an optimal balance between absolute micrometric precision, execution speed, and data robustness.

3.1 Laser triangulation

Laser triangulation is an active non-contact measurement technique that determines the exact position of an object in three-dimensional space using the geometric properties of triangles. The instrument consists of two main components mounted at a fixed distance: an emitter, usually a laser diode, and a receiver, typically a high-resolution CMOS or CCD image sensor.

The operating principle relies on simple trigonometry and the geometric similarity between triangles [11], allowing the system to map the depth profile of a surface by analysing the optical deviation detected on the two-dimensional sensor. The main measurement triangle is formed by a fixed baseline, representing the exact physical distance between the laser emitter and the sensor lens, and the two light paths connecting these components to the illuminated point on the tool. When

the laser hits the cutting edge, any change in surface depth causes the reflected beam to shift; the camera lens then projects this shift onto the image sensor, creating a smaller internal triangle that is geometrically similar to the external one. Due to this strict mathematical proportion, the exact pixel position of the illuminated spot on the sensor provides the angle needed to calculate the absolute depth of that specific point.

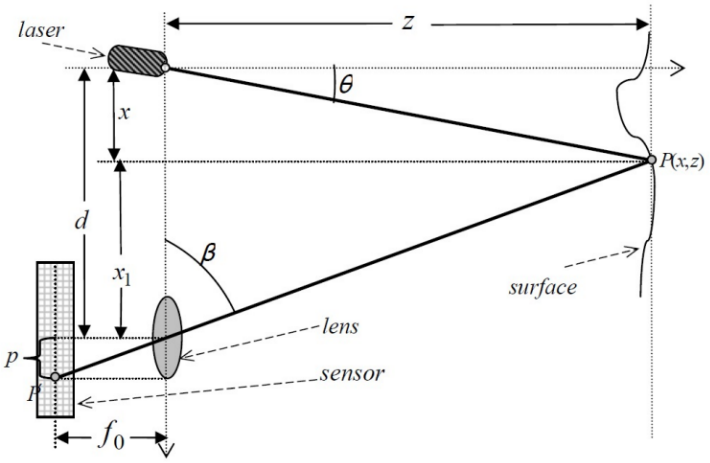

Figure 3.1: Geometry of the laser triangulation principle.

To determine the depth coordinate Z, which represent the actual distance between the instrument and the cutting tool surface, the fixed baseline is geometrically expressed as the sum of the horizontal projections derived from the two optical angles. Defining θ as the projection angle of the laser beam and β as the angle at which the reflected light strikes the sensor, the system's geometry is governed by the following equation:

$$d = z \cdot \tan(\theta) + z \cdot \cot(\beta) \tag{3.1}$$

From this fundamental relationship, since the fixed construction parameters of the sensor (baseline b and projection angle θ) are known, and the dynamic angle β is detected through the position of the illuminated pixel on the receiver, the unknown depth variable Z can be mathematically isolated:

$$z = \frac{d}{\tan(\theta) + \cot(\beta)} \tag{3.2}$$

To move from measuring a single spatial point to a complete three-dimensional reconstruction, modern industrial scanners project a continuous laser line instead

of a single dot [12]. In this configuration, the depth calculation described above is done simultaneously for each point forming the projected laser line, creating a highly detailed depth profile that describes a specific cross-section of the cutting edge. By mechanically sweeping this line across the cutting tool, the system calculates the spatial coordinates for thousands of adjacent profiles at once, generating a dense point cloud to precisely map the entire micro-geometry of the component.

Using laser triangulation in tool presetting offers specific metrological advantages and challenges: in terms of performance, this technology guarantees micron-level accuracy, allowing the topography of functional surfaces, like the rake face and flank face, to be mapped much faster than traditional tactile methods. Furthermore, unlike passive vision systems, the laser architecture does not require the target tool to possess a specific surface texture or color, as the instrument actively projects its own optical reference for measurement.

However, the effectiveness of laser triangulation depends on managing specific physical limitations [13]. The main geometric problem is the shadowing effect, where areas of the cutting edge physically block the light or hide the reflection point from the camera due to the fixed angle between the emitter and the receiver. To overcome this, the system can be scaled up because it relies on simple mathematical principles, allowing the implementation of multiple cameras or sensors that view the same point from different angles. This configuration can fill any optical information gap, ensuring a complete spatial reconstruction even when dealing with complex tool geometries and deep undercuts.

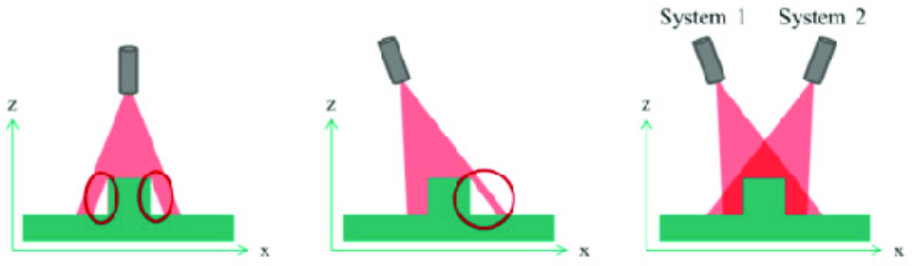

Figure 3.2: Multi camera laser triangulation architecture designed to overcome optical occlusions [14].

The optical properties of the surfaces under examination present a far greater challenge, as cutting tools have highly reflective metallic finishes. When the laser beam hits these polished areas, the light is reflected sharply in a single direction

rather than being scattered evenly. This specular reflection creates two opposite problems: the optical sensor can either be blinded by intense light that saturates the pixels, or it can receive no signal if the beam is reflected away from the lens, causing gaps in the point cloud. Furthermore, the coherent nature of laser light that interact with metallic surfaces can generate speckle noise, a granular optical interference that reduces the resolution of the acquired profile.

Finally, the success of the three-dimensional measurement depends heavily on the mechanical handling system. While the laser scanner provides high point density and micrometric precision within its specific light-blade plane, the overall volumetric accuracy of the scan depends entirely on the kinematics of the setup. Since the complete cutting edge is reconstructed by moving the sensor along the tool axis, any mechanical uncertainty, structural vibration, or straightness errors prevent the correct spatial positioning of each acquired section. Therefore, the performance of the system does not depend only on on the optical instrument, but also on the absolute accuracy of the movement axes and their ability to maintain precise data synchronization during the scan.

To validate the use of the 3D technology and ensure that the sensor meet the project requirements, a technical analysis was conducted on the products from iMAGE S's main suppliers. The investigation focused on three key partners: LMI Technologies [15], Teledyne [16], and AT Sensor [17].

The following table details the main technical parameters of the models that are suitable for integration.

Technical Parameter	**LMI Technologies**	**Teledyne**	**AT Sensor**
X resolution [μm]	2 to 17	3 to 15	5 to 35
Z repeatability [μm]	0.2 to 0.4	0.3 to 0.5	0.2 to 0.9
Field of View [mm]	10 to 30	15 to 32	10 to 100
Clearance distance [mm]	17 to 60	32 to 33	30 to 170
Measurement range [mm]	6 to 25	4 to 15	10 to 60

Table 3.1: Comparative analysis of three dimensional laser profiler specifications.

The data shows that the analysed instruments offer a good balance between precision and flexibility, making them suitable for machine integration. Specifically, the high X-axis resolution guarantees very dense spatial sampling along the laser

line. Keeping this parameter in the micrometer range is essential to detect tiny defects or micro-chips along the cutting edge. At the same time, the high Z-axis repeatability defines the sensor's great depth sensitivity, which is the most critical factor for the entire project, as the physical ability to reliably discriminate sub-micrometric variations along the optical axis.

Regarding the field of view, the compact dimensions offered by these models are strategically optimized for micro-mechanical inspection. A narrow reading width allows the entire optical density of the CMOS sensor to be concentrated exclusively on the faces of the tool, maximizing the number of useful data points without wasting pixels on irrelevant areas like the shank or spindle.

Beyond optical performance, the geometric parameters for hardware integration are also crucial. An adequate clearance distance (the physical space between the sensor lens and the workpiece surface) ensures enough margin, which is essential to avoid collisions during tool rotation or the rapid movement of the CNC axes. Finally, a wide measurement range defines the depth of field within which the sensor maintains its accuracy, enabling the scanning of deep profiles without continuously repositioning the sensor.

3.2 Structured Light

Structured light three-dimensional scanning is an area-based active optical measurement technique. Instead of mechanically sweeping a single laser line across the target, structured light systems project a complete two-dimensional light pattern onto the entire surface of the object at once, using a hardware architecture that consists of a central digital projector flanked by one or more high-resolution cameras positioned at fixed angles.

The operating principle is based on the fundamental geometry of active triangulation, sharing its theoretical foundation with laser scanning, as both methods evaluate the optical distortion of a projected light source observed from a fixed angle. However, structured light architecture captures spatial data in a different way. While a laser system relies on the mechanical movement of the sensor to map an area line by line, structured light reconstructs the geometric entirely through optical encoding [18]. The projector casts a rapid sequence of known geometric patterns (typically alternating light and dark parallel stripes) directly onto the cutting tool. This technique, known as fringe projection, simultaneously illuminates the entire field of view with straight geometric fringes that exhibit optical distortion when striking the complex three dimensional topography of the

cutting edge.

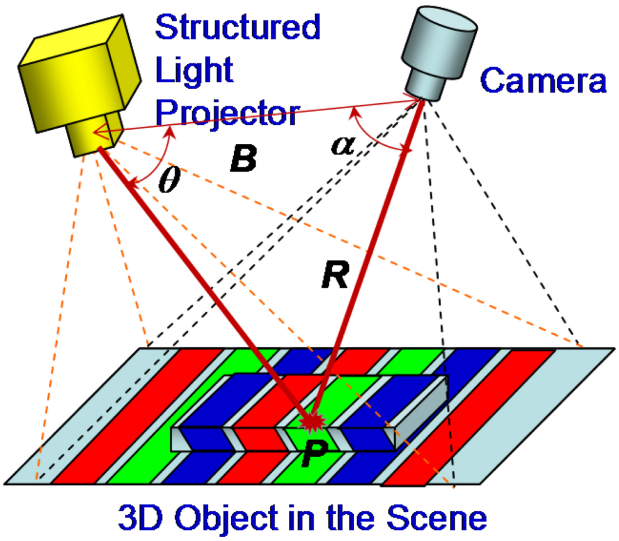

Figure 3.3: Structured light projection principle.

The cameras capture this deformation, which is directly proportional to the depth, inclination, and curvature of the tool surfaces. By analysing how the sequence of patterns changes locally, the measurement software mathematically solves the optical correspondence problem for millions of pixels simultaneously.

To calculate the exact spatial coordinates of the acquired points, the system relies on trigonometric principles [19]. Since the fixed baseline distance B between the optical center of the projector and the camera is known, the software can determine the absolute distance R of a specific point on the tool surface using the following equation:

$$R = B \cdot \frac{\sin(\theta)}{\sin(\alpha + \theta)} \tag{3.3}$$

In this equation, θ is the projection angle of the light fringe, and α is the reception angle detected by the camera. This mathematical correlation allows the system to calculate the spatial coordinates of the entire framed area in a single scan, eliminating the need to move the sensor along the machine axes. Furthermore, to achieve the sub-micrometric accuracy required in modern tool presetting, these high-resolution systems use phase-shifting techniques. By shifting the stripe pattern by microscopic fractions of its width and capturing multiple images of these offset fringes, the software calculates the depth value for every pixel, generating a dense and accurate point cloud.

Using structured light in tool presetting offers metrological advantages [20] mainly related to acquisition speed and spatial data density. Since it is an area-based technique, the system can capture the complete three-dimensional geometry of the cutting edge in a single shot. This simultaneous acquisition of millions of points drastically reduces inspection time compared to laser scanning. Furthermore, the absence of mechanical movement during the scan eliminates any potential error introduced by machine vibrations or axis kinematics. Despite these benefits, structured light systems have operational limits that must be evaluated like their sensitivity to ambient light, especially compared to laser profiling. While laser emitters concentrate an intense beam that is easily isolated with narrow-band optical filters, structured light relies on small contrast differences across a wide projection. Because of this, external light or environmental reflections can easily interfere with the fringe pattern, reducing contrast and degrading measurement accuracy.

Furthermore, structured light shares a major limitation with laser triangulation regarding the optical properties of cutting tools: since solid carbide and ground steel surfaces are shiny and highly specular, the structured light pattern reflects unevenly of these polished metallic finishes, just like a laser line. This specular reflection saturates the camera pixels in bright areas while scatters light away from others, leaving them completely dark and preventing the software from decoding the pattern [13]. As a result, both optical technologies often suffer from missing data points and incomplete reconstructions along the functional faces of the tool.

To validate the structured light technology and evaluate its practical feasibility, the technical datasheets of the Gocator snapshot series by LMI Technologies [15] were analysed. The following table summarizes the absolute specifications of the evaluated models.

Technical Parameter	**Model 3210**	**Model 3506**	**Model 3520**
Resolution XY [μm]	60.0 to 90.0	20.0 to 25.0	74.0 to 121.0
VDI/VDE Accuracy [μm]	35.0	12.0	90.0 to 200.0
Field of View [mm]	71.0 × 98.0 to 100.0 × 154.0	27.0 × 45.0 to 30.0 × 45.0	179.0 × 115.0 to 282.0 × 175.0
Clearance distance [mm]	165.0	87.0	203.0
Measurement range [mm]	110.0	25.0	150.0

Table 3.2: LMI snapshot sensors technical specifications.

The data provided highlight the main trade-off of structured light sensors. Although area-based acquisition is very fast, the XY resolution and VDI/VDE accuracy show lower precision compared to laser profiling. While, the XY resolution can capture the tool's macro-geometry it lacks the micrometer-level density needed to reliably detect tiny defects or micro-chips along the cutting edge. Similarly, the VDI/VDE accuracy values indicate lower depth sensitivity on the Z-axis, making it harder to distinguish sub-micrometer variations and complicating the reconstruction of the slight slopes of the rake and flank angles.

Regarding the field of view, the models show an inverse relationship between the framed area and measurement precision: while a wider reading window captures a large portion of the tool in a single shot to drastically optimize the scan time, spreading the camera's fixed resolution over a larger surface dilutes the spatial resolution. This limits the ability to focus the acquired points exclusively on the functional faces of the cutting edge, wasting pixels on irrelevant areas and reducing point cloud density where it is needed most.

Beyond optical performance, looking at the geometric parameters for hardware integration reveals the main limit of snapshot systems. While a sufficient clearance distance ensures safe scanning, and a narrower field of view can improve resolution, a metrological gap remains. Even when these spatial parameters are perfectly optimized, structured light technology cannot match the micrometric accuracy of laser triangulation, making it, despite the speed of area based acquisition, less suitable than laser profiling for certifying the strict tolerances required on the cutting edge.

3.3 Stereovision

Stereoscopic vision technology, commonly called stereo vision, is an optical measurement technique inspired by human binocular perception [21]. The basic hardware architecture consists of two digital cameras positioned side by side at a fixed and known horizontal distance, defined as the baseline.

Similar to human eyes, the two cameras simultaneously capture 2D images of the same object from slightly different perspectives. Since the two lenses observe the target from different viewpoints, the position of a specific point will appear shifted between the left and right images due to the parallax effect[1] [22]. To extract depth information from this effect, the algorithm must solve the spatial correspondence problem by identifying the exact same points across both images. Once the software identifies a pair of matching pixels, it proceeds to calculate their disparity [23], a metric defined as the horizontal positional difference in pixels between the coordinates of the same point in the first and second images.

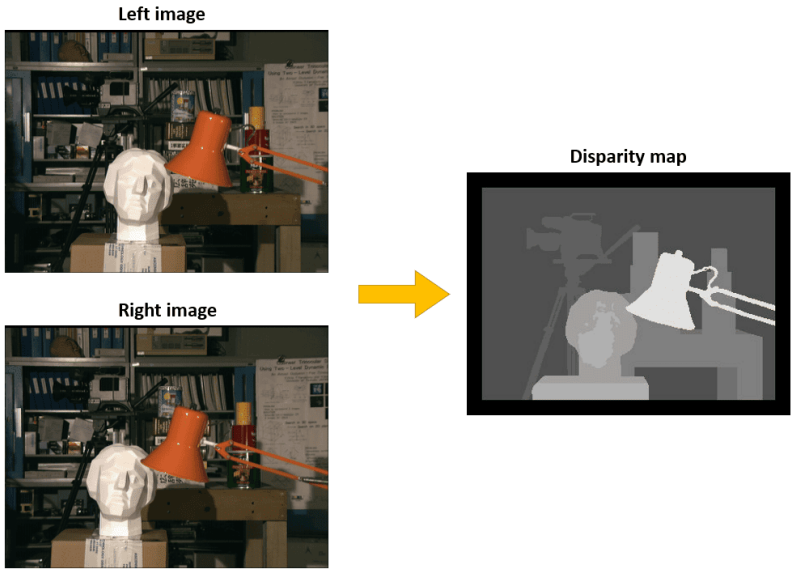

Figure 3.4: Generation of a disparity map from a stereoscopic image pair.

By aggregating these displacement values to generate a disparity map, the system uses optical triangulation to compute the depth of each individual point.

[1]Parallax effect: The apparent displacement of an object when viewed from two different positions; the closer the object is to the observer, the greater this displacement becomes.

Because the depth along the Z axis is mathematically inversely proportional to the measured disparity, it can be computed using the following equation [24]:

$$Z = \frac{f \cdot B}{d} \tag{3.4}$$

In this equation, f represents the focal length of the lenses in pixels, B denotes the physical baseline between the optical centers of the two cameras, and d is the calculated disparity. By applying this relationship, the system is able to convert the 2D images into a dense 3D point cloud.

Using stereo vision in industrial environments offers several advantages compared to other depth-sensing methods [21]. A major strength of this technology is its robust performance in areas with high ambient brightness, where infrared-based systems often experience significant noise. Moreover, because stereo vision uses standard high-resolution image sensors, it can generate a highly detailed three-dimensional reconstruction at a relatively low hardware cost. Finally, the highly flexible architecture allows depth sensing over long ranges by simply adjusting the baseline distance.

Despite these strengths, passive stereo systems also present a major limitation: their complete dependence on the visual texture and illumination of the targeted scene. Because the correspondence algorithm operates by identifying unique features and intensity gradients across the captured images, it demands optimal environmental conditions to ensure accurate pixel matching. Furthermore, calculating dense disparity maps remains highly computationally intensive, requiring dedicated processing units to sustain acceptable frame rates during real time monitoring.

Inspecting objects characterized by homogeneous or highly reflective surfaces presents a particularly difficult challenge. In the specific case of metal cutting tools, materials such as solid carbide or polished steel often appear visually uniform, lacking the natural contrast required for accurate pixel matching. Under these conditions, a passive system struggles to identify corresponding points across the stereo image pair, generating a low density or incomplete point cloud that fails to satisfy strict metrological standards. To solve this problem, active stereo vision uses a specialized light projector that overlays a structured pattern or a pseudo-random texture directly onto the object. By providing these artificial visual features, the projector helps the software to identify precise correspondences even on highly homogeneous surfaces, ensuring reliable data acquisition regardless of the specific optical properties of the material.

Considering the previously discussed advantages and physical limitations, examining commercial sensors helps define the practical performance of stereo vision. By analysing how different technical parameters dictate depth accuracy and measurement volume, it is possible to identify the geometric constraints typical of these systems. This comparative approach highlights the fundamental relationships between focal length and distance, providing a clear overview of current capabilities in high precision three dimensional reconstruction. The data presented below illustrates these specifications by comparing several models developed by by IDS [25].

Technical Parameter	**B57 4**	**C57 S**	**C57 M**	**X36 5CP**
Z Accuracy [mm]	0.1 at 300.0	0.1 at 975.0	0.2 at 1850.0	0.3 at 1700.0
Focus distance [mm]	350.0	975.0	1850.0	1700.0
Focal length [mm]	4.0	4.0	4.0	8.0
Working distance [mm]	210.0 to 2000.0	500.0 to 5000.0	650.0 to 5000.0	1700.0
Measurement range [mm]	1047.0 to 1573.0	991.0 to 1495.0	1304.0 to 1807.0	1363.0 to 1865.0

Table 3.3: Ensenso stereo sensors performance specifications.

The performance metrics reveal that while active stereo vision is a versatile technology for various industrial applications, its depth resolution is a limiting factor for high-precision metrology. According to the data, even the most accurate models achieve a Z-axis accuracy of only 0.1 millimeters under optimal conditions. While this level of detail is sufficient for robotic guidance, bin picking, or general object recognition, it is not enough for the strictly micrometric standards required for tool presetting. Measuring a cutting edge demands single digit micrometer accuracy to correctly capture the precise slopes of the rake and flank angles. Consequently, despite its robustness across different materials, stereo vision introduces a severe optical bottleneck.

3.4 Depth-From-Focus

Depth-from-focus technology is an optical metrology method that reconstructs the three-dimensional topography of an object using a single-camera system. This technique relies on the concept of depth of field [26], which is the specific spatial range along the optical axis where an object appears sharp. While a large depth of field is desired in standard photography, the depth-from-focus architecture uses optical lenses with an extremely shallow depth of field; this physical restriction ensures that only a narrow slice of the target is perfectly in focus at any given moment, while the rest appears blurred.

Once the scan is complete, the software analyses the entire image sequence to extract the spatial coordinates, applying a focus measure operator to quantify the blur across the dataset. This function evaluates intensity gradients between adjacent pixels, since a perfectly focused physical detail naturally exhibits sharp transitions and high contrast, whereas a blurred region presents smooth and uniform pixel values. By calculating this contrast metric for every pixel across all frames, the system generates a focus profile along the Z-axis.

To achieve a better precision, the algorithm does not just select the image frame with the highest contrast score. Since the vertical movements along the Z-axis occur in discrete steps, the plane of maximum sharpness might lie between two captured photos. To solve this, the software fits a mathematical model, like a Gaussian curve, to the contrast values of adjacent frames. The peak of this curve then identifies the exact focal point, ensuring micrometric accuracy even between the mechanical steps of the translation stage [27].

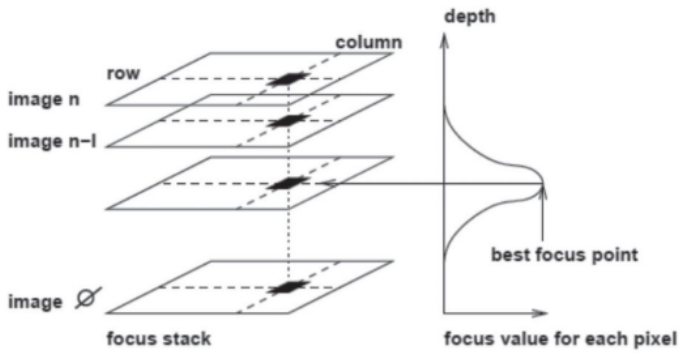

Figure 3.5: Determination of the exact focal point using contrast curve fitting across multiple image planes.

Once these focal peaks are determined across the sensor matrix the algorithm assigns the corresponding Z-axis coordinates to each pixel, reconstructing the complete three dimensional topography of the object [28]. While this method provides high measurement precision, it introduces a trade-off in acquisition speed. Since the hardware must capture and the software must process a large stack of images, the execution time is much longer than with single-shot technologies. In this method, there is a direct correlation between dataset size and accuracy; while processing a higher number of frames delivers better geometric precision, it consequently demands much longer computational times. Despite this slow speed, depth-from-focus is very useful in microscopy applications where small objects and intricate details must be magnified. Instead, for macroscopic evaluations with a wider field of view (up to 100 mm), alternatives like stereo vision or laser triangulation are often preferred because they are faster and require fewer frame acquisitions.

To evaluate the performance and limits of depth-from-focus technology, several commercial products must be examined. By analysing the technical specifications of industry-leading metrology instruments, such as the optical sensors manufactured by Alicona [10], it is possible to quantify the actual capabilities of this measurement approach. The following table summarizes the core performance metrics of various models.

Technical Parameter	**IF Sensor R25 10x**	**IF Sensor R25 2xSX**	**EdgeMasterX 2xSX**
Working distance [mm]	17.5	34.0	34.0
Field X Y [mm]	2.0×2.0	10.0×10.0	10.0×10.0
Vertical resolution [μm]	0.10	3.5	3.5
Min. measurable radius [μm]	5.0	20.0	20.0

Table 3.4: Alicona sensor specifications.

The numerical data in the table supports the theoretical principles discussed earlier. The main advantage of this technology is its vertical resolution, reaching down to 0.10 micrometers for the most precise models, making these sensors ideal for analysing microscopic surface roughness, potentially providing the exact depth sensitivity needed to evaluate the delicate rake and flank angles of industrial tools. However, the data also shows the limits of depth-from-focus: to achieve such vertical precision, the XY measurement field is greatly reduced, often covering

an area of just few square millimeters. Furthermore, acquiring and processing a dense sequence of focal planes for such a restricted field of view drastically increases execution times. Because rapid and comprehensive tool presetting is a primary requirement for this project, the combination of a limited inspection area and slow processing speeds creates a critical bottleneck. Consequently, despite its high accuracy, these operational constraints raise doubts about using it as the primary 3D measurement system, a factor that will be considered in the final technology selection.

3.5 Confocal

Confocal measurement technology is the final advanced optical approach for three-dimensional surface reconstruction examined in this analysis. The operating principle of a confocal sensor relies on an optical setup designed to eliminate out-of-focus light [29]. In this architecture, a point light source (typically a laser or a LED) is projected through an objective lens onto the target's surface. The reflected light then travels back through the same optical path and is redirected by a beam splitter toward a light detector.

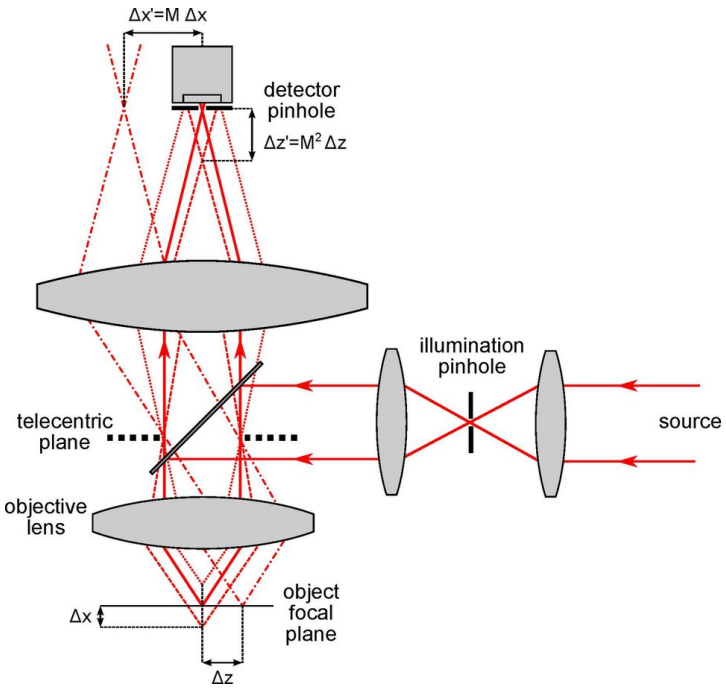

Figure 3.6: Optical architecture of a confocal sensor for high-precision depth measurement.

The key component of this technology is a spatial filter, or pinhole, placed at the conjugate focal plane of the detector. This geometry ensures that only light rays reflecting from the exact focal point pass through the pinhole to reach the sensor, while any scattered light or reflections from above or below the focal depth are blocked by the pinhole's edges [30].

Consequently, the detector records a maximum intensity signal only when the surface intersects the focal plane. However, because the system isolates a single point at a time, the hardware must scan the target to generate a complete three-dimensional map. By sweeping along the Z-axis, the software records the height at which the intensity peak occurs for every coordinate on the XY plane, reconstructing the full geometry of the tool.

In industrial metrology, confocal architecture offers specific advantages: one of the most notable advantages is its exceptional ability to measure surfaces with extremely steep angles and severe slopes. Furthermore, confocal sensors perform well on highly reflective metallic materials, ensuring a clean optical signal without the specular noise that typically compromises traditional triangulation systems.

Despite these optical capabilities, the technology is heavily penalized by its scanning mechanics [31]: since it evaluates a single point at a time, the system must perform a complete point-by-point scan across both the XY plane and the Z-axis to reconstruct a three-dimensional volume. This sequential data acquisition process is very slow, making scanning time a major drawback.

In addition to the slow operational speed, the high optical magnification required for confocal measurement results in a small field of view. To map larger areas, the system must capture and stitch multiple images together, further increasing the total measurement time. For a tool presetting machine like the Speroni system, which requires a rapid evaluation of the entire tool geometry, this combination of a small measurement window and a slow scanning rate constitutes a severe operational bottleneck. Consequently, these profound limitations will be weighed against the technology's high accuracy during the final selection phase to determine its overall viability.

To evaluate the capabilities and limits of confocal technology, an analysis of commercial sensors is required, examining the specifications of advanced models translates theoretical principles into practical values. The following table outlines the main parameters of several confocal systems to evaluate their suitability for tool presetting [15].

Technical Parameter	**Model 4010**	**Model 4011**	**Model 4020**	**Model 4021**
Resolution X [μm]	1.9	1.9	2.6	2.6
Linearity Z [± % of MR]	0.04	0.04	0.02	0.02
Resolution Z [μm]	0.25	0.20	0.50	0.40
Repeatability Z [μm]	0.12	0.10	0.25	0.20
Field of View [mm]	3.5	3.5	5.0	5.0
Clearance distance [mm]	9.3 ± 0.2	9.3 ± 0.2	27.8 ± 0.3	27.8 ± 0.3
Measurement range [mm]	1.05	1.05	2.5	2.5

Table 3.5: Confocal sensors performance.

The data in the table support the theoretical limitations discussed earlier. The vertical accuracy is very precise, with the Z-axis resolution reaching sub-micron values as low as 0.20 micrometers in the most advanced models. This precision, combined with a repeatability of 0.10 micrometers, ensures an accurate 3D reconstruction of the cutting edges, providing the depth sensitivity needed to evaluate rake and flank angles.

However, this vertical accuracy is tied to a very small field of view, which means that to inspect an entire cutting tool, the optical head would need to perform many overlapping scans. Because the confocal architecture relies on a point-by-point data acquisition process, this small field of view increases the total execution time. Therefore, despite providing the highest measurement quality, despite its high measurement quality, confocal technology is too slow and geometrically limited for a modern tool presetting machine like the Speroni system

3.6 Comparative Analysis

Selecting the best optical system for an industrial tool presetting machine requires a careful evaluation of multiple competing factors. As shown in the previous sections, no single 3D measurement method excels in every technical parameter: technologies with sub-micrometer Z-axis precision, like confocal microscopy or depth from focus, are limited by a tiny field of view and very slow processing times, and approaches like stereo vision or structured light provide fast scans over large areas, but they lack the vertical accuracy needed to measure the rake and flank angles.

To make an objective decision, the technical specs and operational features of all analysed methods are summarized below. The following table compares the average performance, advantages, and limits of each technology.

Feature	**Laser Triangulation**	**Structured Light**	**Stereo Vision**	**Depth from Focus**	**Confocal**
Z accuracy [μm]	0.2 to 10	1 to 20	100 to 300	0.1 to 3.5	0.2 to 0.5
X Y accuracy [μm]	2 to 35	5 to 50	50 to 200	1 to 5	1.9 to 2.6
FOV [mm]	10 to 100	50 to 500	100 to 1000	1.6 to 10	3.5 to 5.0
MR [mm]	4 to 60	20 to 200	50 to 500	1 to 20	1.05 to 2.5
CD [mm]	17 to 170	100 to 500	100 to 1000	17 to 37	9.3 to 27.8
Main Advantage	Fast scanning	Full area capture	Flexible large area	Coaxial precision	Steep slopes
Main Limitation	Shadow occlusion	Reflection issues	Texture dependent	Slow stack processing	Point by point scan

Table 3.6: Comparison of 3D measurement technologies.

By evaluating the data in the comparative table, we can identify the best architecture for the project. The alternative methods are discarded for the following reasons:

- **Stereovision:** While it captures large areas in a single shot, its spatial resolution cannot provide the micrometric accuracy needed to inspect the rake and flank angles.
- **Depth from focus and confocal microscopy:** These offer high vertical resolution, and confocal systems handle reflections well. However, point-by-point scanning or focal stacks make them too slow. Additionally, their

tiny measurement range is incompatible with the size of standard industrial tools, making them unsuitable for fast geometric analysis.

- **Structured light:** This method provides lower accuracy than a high-end laser setup, and its projected optical patterns are disrupted by specular reflections from shiny metal surfaces.

This leaves laser triangulation as the best choice for the project. The main limitation of a 3D laser profiler is the need for highly precise movement between the sensor and the target. However, the mechanical architecture of the machine solves this problem, since the Speroni equipment already uses highly accurate motorized axes to move and rotate the tool the mechanical translation is provided without adding structural complexity. By leveraging this movement, the laser sensor can quickly sweep across the tool to generate an accurate 3D point cloud, offering the best balance between fast scanning speed, a wide measurement range, and the micrometric accuracy required to certify cutting tools.

Chapter 4

Preliminary Sensor Validation

The comparison of the three-dimensional acquisition technologies presented in chapter 3 identified laser triangulation as the most suitable optical architecture to meet the precision and resolution requirements of the project. Following these theoretical conclusions, the research moved to a preliminary experimental phase to validate the chosen technology, focusing on the metrological evaluation of the laser triangulator to verify measurement accuracy, system repeatability, and operational reliability.

This validation process was carried out through an industrial collaboration with the companies iMAGE S and Speroni. While iMAGE S, a specialist in machine vision applications, provided the technical support and the laboratory environment needed to perform the preliminary optical tests, Speroni defined the strict metrological requirements and supplied the real mechanical tool samples used for the experimental trials. The purpose is to verify if the laser triangulation method maintains its theoretical performance when dealing with the complex geometries and highly reflective surfaces typical of industrial milling cutters.

To perform these topographical analyses, iMAGE S supplied an LMI Gocator 2520 laser profiler, which was chosen for its technical specifications (shown in fig. 4.1) since its optical resolution and field of view are perfectly compatible with the strict dimensional tolerances required by the automated tool presetting project.

QUICK SPECS

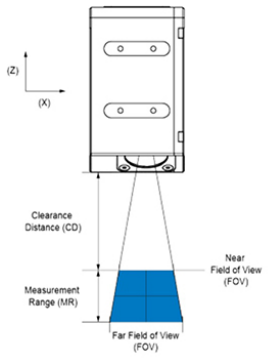

Model	2510	2512	2520	2522	2530
Resolution X (mm)	0.008	0.008	0.013 - 0.017	0.013 - 0.017	0.028 - 0.054
Field of View (mm)	13.0 - 14.5	13.0 - 14.5	25.0 - 32.5	25.0 - 32.5	48 - 100
Clearance Distance (mm)	17.0	17.0	47.5	17.75	40.0
Measurement Range (mm)	6	6	25	25	80
Laser	Blue	Blue	Blue	Blue	Blue
Datasheet	PDF	PDF	PDF	PDF	PDF

Figure 4.1: Gocator® 2500 Series – Quick Specs

The experimental activity detailed in this chapter focuses on characterizing the sensor's performance by identifying and evaluating the variables that impact measurement quality, which is an essential step to validate the system before its final integration into the target machine.

4.1 Materials and Methods

For the preliminary tests, a test bench was set up at the iMAGE S laboratory to simulate the working conditions of a quality control system by fixing the laser profiler vertically, with its optical axis perpendicular to the measurement plane, while the sample was placed on a motorized linear slide moving at a constant speed (fig. 4.2). This configuration, with a static sensor and a moving part, was used to generate a three-dimensional scan of the profile along the feed axis, ensuring good geometric accuracy and repeatability.

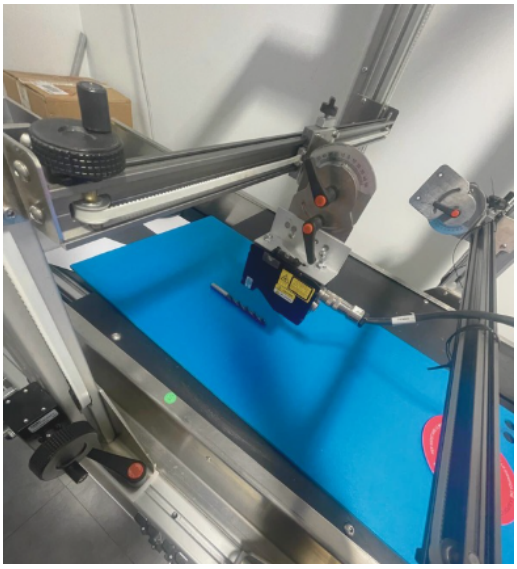

Figure 4.2: Experimental setup for the preliminary scans.

However, from the initial scans, a stability issue with the motion system was noticed, as analysing the raw data from flat reference surfaces showed abnormal variations in the vertical distance linked to the mechanical limits of the slide. After a check with the laboratory staff, it was confirmed that the linear slide had some mechanical play and vibrations while moving. Even though these oscillations are in the order of fractions of a millimeter and are usually fine for standard industrial vision applications, they are not compatible with the micrometric tolerances needed to characterize the cutter edges.

To quantify the systematic error introduced by the motion system, a geometric analysis was performed on the section of the cutter clamped in the spindle (fig. 4.3), which, since it is not used for cutting, maintains its original high-precision cylindrical shape and serves as a perfect reference to verify the setup's stability.

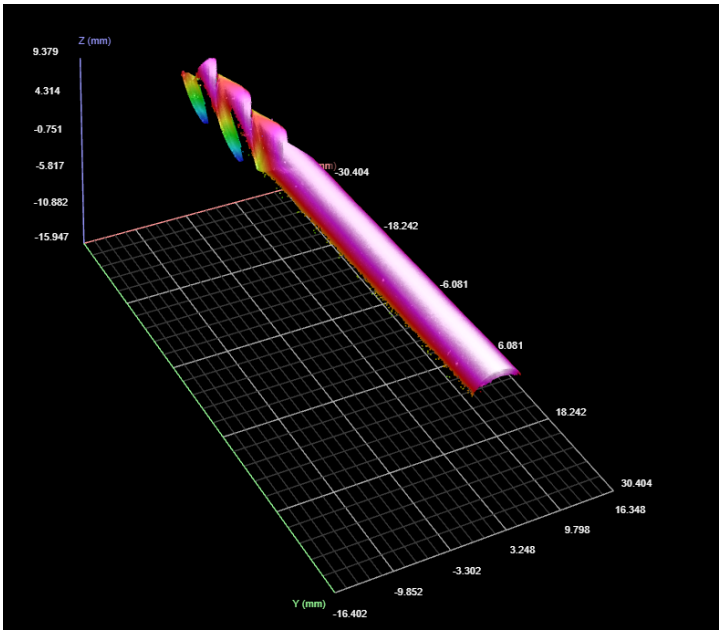

Figure 4.3: Example of the scanned cutter.

Specifically, two cross-sections of the profile were extracted at a known distance Δy along the scanning direction, and because of how laser triangulation works (the sensor only captures the upper part of the cylinder), the analysis focused on the maximum height found in each section.

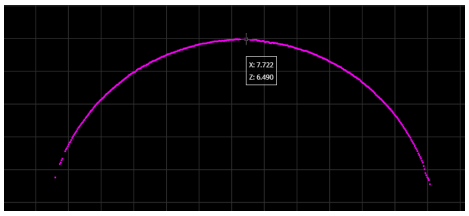

(a) Cross-section at $y = 24.282$ mm

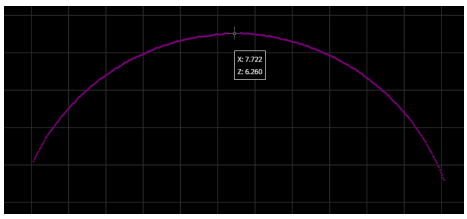

(b) Cross-section at $y = -8.075$ mm

Figure 4.4: Comparison of the two acquired profiles on the cylindrical shank.

By calling the maximum heights in the two sections z_1 and z_2, the total height variation was calculated as:

$$|\Delta z| = |z_2 - z_1| = |6.260 - 6.490| = 0.230$$

Looking at the two sections in fig. 4.4, taken at a distance Δy of 32.357 mm from each other, the systematic drift per unit of length d was found as follows:

$$d = \frac{\Delta z}{\Delta y} = \frac{0.23 \text{ mm}}{32.357 \text{ mm}} \approx 0.00711 \text{ mm/mm} = 7.11 \mu\text{m/mm} \tag{4.1}$$

These results show that for every millimeter of travel, the height measurement has a systematic drift of about 7.11 μm. Since this error grows linearly with the distance, it is clearly due to a structural misalignment or mechanical limits of the motion system, rather than actual defects on the workpiece. This confirms that the current setup cannot guarantee the needed micrometric accuracy over large surfaces, making it necessary to use a more stable positioning system to properly characterize the cutting.

Since we could not fix the mechanical error at this stage, the validation strategy had to change, putting the analysis of absolute accuracy on hold to focus first on verifying the sensor's precision and stability. This method is based on the metrological difference between accuracy and precision, also known as repeatability [32]. While the main goal in an ideal measurement system is to minimize the total error coming from a mix of systematic error (bias) and random error [33], the mechanical limits of the motion system in our setup introduce a large systematic error.

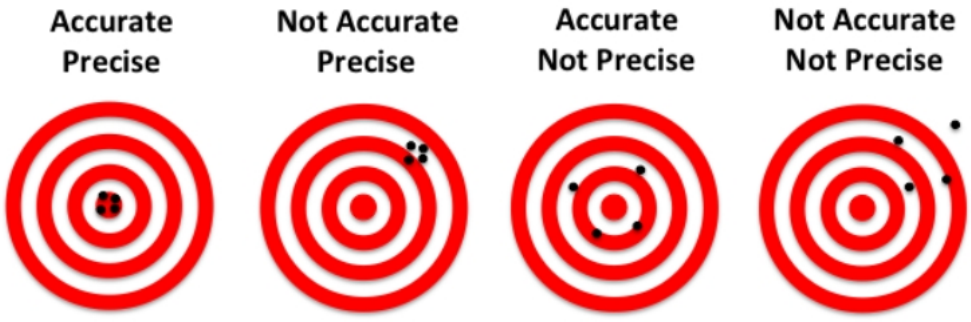

Figure 4.5: Accuracy and precision comparison.

Specifically, mechanical play and vibrations cause the measured average value to shift from the true value, compromising the overall accuracy. Even so, this problem does not stop us from evaluating the profiler's ability to give consistent and repeatable measurements over time, since we can isolate the quality of the sensor's data from the external positioning errors.

The idea behind this approach is that a good metrological instrument must guarantee high precision, regardless of any systematic bias or external noise caused by the movement. Because of this, the experimental work shifted towards repeatability tests to check the differences between successive scans taken under the exact same conditions. The main goal is to characterize the sensor's intrinsic random error, which can be seen as internal noise, by showing that the instrument can generate dense and overlapping point clouds with low dispersion and a small standard deviation σ. This isolates the performance of the Gocator 2520 from the mechanical uncertainties, making data stability validation the first step for a future system calibration; if the error is constant and predictable, it can be easily compensated once the structural limits of the test bench are fixed.

To do this analysis properly, we had to use a certified geometric reference. Since a metrological evaluation needs a comparison with a ground truth, the tests on complex tools were preceded by tests on gauge blocks (Johnson blocks). These standards act as ideal flat surfaces, allowing us to verify with high precision how much the sensor's readings deviate from the theoretical reference, which provides a solid baseline for characterizing the cutting edges later on. The tests involved scanning gauge blocks with heights of 1, 2, 5, and 10 mm, chosen to observe the sensor's behavior at various working distances within its measuring range and to make sure the instrument's response stays constant regardless of the object's thickness. Since certified gauge blocks provide a known geometry and guaranteed flatness, the acquired profiles were fitted to a linear model using a regression line that minimizes the distance between the measured points and the theoretical surface.

This regression line works as an ideal reference to precisely evaluate the scan's precision, making it possible to run repeatability analyses and quantify instrumental errors by measuring how much each point deviates from the reference line. To make these assessments objective and comparable, three main statistical indicators were chosen to evaluate the distribution and size of these deviations: Mean Absolute Error (MAE), Root Mean Squared Error (RMSE) [34], and the standard deviation (σ) of the residuals [35]. These parameters give a complete characterization of the sensor's precision, identifying its sensitivity to random noise and possible outliers during the scan.

The first parameter is the Mean Absolute Error (MAE), which measures the average deviation of the acquired points. It is calculated as the mean of the absolute differences between the measured values z_i and the predicted ones $\hat{z}_i$, providing a direct estimate of the average error regardless of its direction:

$$MAE = \frac{1}{n}\sum_{i=1}^{n}|z_i - \hat{z}_i| \tag{4.2}$$

The second indicator is the Root Mean Square Error (RMSE), which is very useful for identifying signal instability. By squaring the deviations, it gives more weight to larger errors; therefore, an RMSE value much higher than the MAE suggests that the measurements are affected by noise peaks or outliers that deviate significantly from the linear model:

$$RMSE = \sqrt{\frac{1}{n}\sum_{i=1}^{n}(z_i - \hat{z}_i)^2} \tag{4.3}$$

Finally, the standard deviation (σ) of the residuals was used as the main metric to assess the instrument's precision. It measures the dispersion of the points, showing how closely the measurements are clustered around the fitted model. In metrology, a low standard deviation ensures consistent and repeatable results, which is essential to distinguish the sensor's background noise from the actual shape irregularities of the analysed surface:

$$\sigma = \sqrt{\frac{1}{n-1}\sum_{i=1}^{n}(r_i - \bar{r})^2} \tag{4.4}$$

where r_i is the residual of a single point compared to the regression line, and $\bar{r}$ is the mean of the residuals.

4.2 Planar Reference Analysis

The initial validation phase focused on testing the sensor's performance using certified gauge blocks of 1, 2, 5, and 10 mm. To evaluate the instrument's intrinsic precision, the analysis first looked at single static scans, followed by a second phase that averaged 10 consecutive profiles to check measurement repeatability and quantify the benefits of signal stabilization.

Certified gauge blocks act as a physical reference, providing an ideal theoretical model of a perfectly flat and horizontal surface to validate the measurements against. However, since the sensor captures a discrete set of points, this raw point cloud cannot be directly compared to the theoretical model, making it necessary to extract a single representative line from the acquired points. This is achieved by using a linear regression algorithm to analyse the point cloud and

calculate the straight line (defined by the equation $z = ax + b$) that passes as close to all of them as possible.

In the code, this line is computed using the polyfit function from the NumPy library [36], which applies the ordinary least squares method to find the best fit. Practically, the algorithm calculates the vertical deviation, or residual, between each measured point and the theoretical line, squaring these differences to give more weight to larger errors and ensure all values are positive. The function then finds the slope and intercept that minimize the total sum of these squared errors, providing the best fitting line for the point cloud.

Listing 4.1: Linear fitting using NumPy

```
import numpy as np

# Linear regression to find the slope
coeffs = np.polyfit(x, z, 1)
a, b = coeffs
z_fit = np.polyval(coeffs, x)
```

Once the regression line is calculated, it becomes clear that the profile has a systematic slope, meaning that even though the gauge block surface is nominally flat, the fitted line is not horizontal but noticeably tilted compared to the sensor's measurement axis, as shown in fig. 4.6.

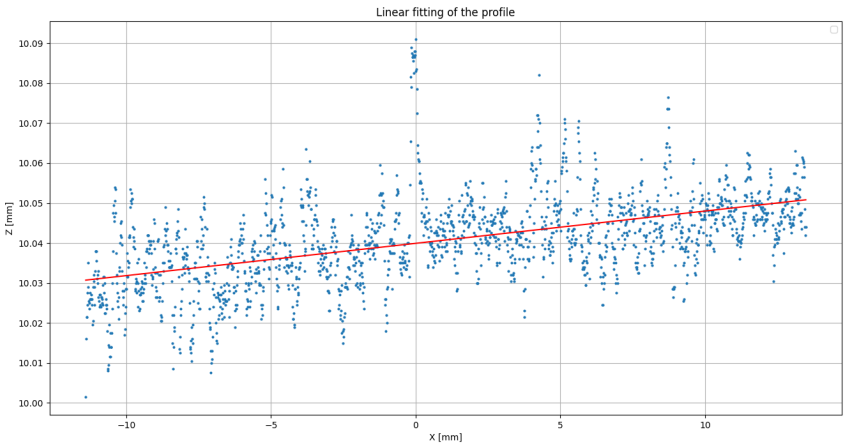

Figure 4.6: Fitted line on the gauge block showing a systematic slope.

This tilt is likely caused by two main mechanical factors: a slight misalignment of the sensor relative to the measurement axis, or a physical tilt of the sliding plane supporting the sample. To fix this issue, we first tried using the Gocator's

onboard processing, as the device acts as a smart camera capable of aligning the scan to a user-defined reference plane. However, this software calibration was not enough during our tests, and the slope remained, meaning the correction had reached its limits, likely due to physical issues in the setup. These limits can be linked to structural factors, because while the main linear slide works with minimal play, other parts of the support structure might introduce vibrations that exceed the micrometric tolerances needed for this application. Additionally, a secondary hypothesis is that the support plane itself might not be perfectly flat, and even a slight concavity could affect the software reference plane, causing the residual tilt seen in the data.

Since the main goal of this work is to validate the sensor's precision rather than redesigning the mechanical setup, a simple reinforcement was added to improve the measurement conditions, making sure the final accuracy assessment reflects the actual performance of the sensor instead of being affected by avoidable structural problems. To do this, the system was stabilized by adding an extra rigid support to create a better mechanical coupling between the sensor and the base, aiming to reduce micro-vibrations and make the structure stiffer so the sample surface stayed aligned with the reference frame. The effectiveness of this extra support is clear in the improved quality of the acquired profiles, as shown in the graph below featuring the scan on the 10 mm gauge block, chosen as an example, after applying the structural reinforcement.

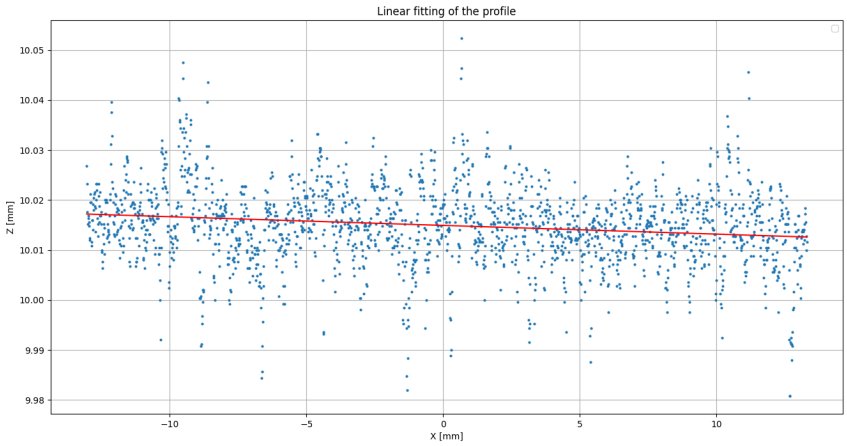

Figure 4.7: Profile scan on the 10 mm block after structural reinforcement.

The improvement in the scan quality can be seen in two ways: first, the linear fit has a noticeably smaller slope compared to the previous setup, showing a better geometric alignment between the sample surface and the sensor; and second, the measured points are distributed more evenly around the fitted line, forming a narrower band. This means the data is more compact and the measurement variability is lower, suggesting that the reinforcement successfully reduced the micro-vibrations that affected the previous scans.

This practical test highlights a key aspect of laser triangulation: the mechanical reliability of the support structure is just as important as the intrinsic resolution of the sensor. In fact, even a simple, empirical stiffening of the setup without a complete redesign was enough to produce a clear improvement in the data, showing that a manual reinforcement can greatly improve stability and proving how important the mechanical infrastructure is for micrometric measurements. A rigid and stable setup is therefore not a secondary detail but a basic requirement for reliable data acquisition, since without it, even high-performance optical instruments cannot reach their nominal accuracy, as mechanical instabilities will inevitably show up in the measurement signal.

4.2.1 Error Distribution

Following these steps, the scan shown in fig. 4.7 was analysed using the metrics introduced earlier. Evaluating the residuals from the single-scan profile gives a quantitative measure of the sensor's intrinsic performance:

- The Mean Absolute Error (MAE) is 0.005710 mm;
- The Root Mean Square Error (RMSE) is 0.007777 mm;
- The standard deviation of the residuals (σ) is 0.007779 mm.

These experimental results give a clear idea of the sensor's accuracy. A standard deviation of about 7.7 μm on a single frame confirms the high metrological performance of the Gocator 2520, even without filtering or temporal averaging. Looking at the error metrics, the RMSE is only slightly higher than the MAE, which is normal for Gaussian-distributed errors. Since the RMSE formula squares the deviations, it gives more weight to larger errors; therefore, the small difference between these two parameters shows that there are almost no outliers or isolated noise peaks, suggesting a clean signal with an even dispersion of points across the entire profile.

While these numerical indices give a quantitative measure of the error, to fully understand it requires to see how these deviations are distributed along the profile. Analysing the residuals shifts the focus from purely statistical data to a visual check of the fitting quality and sensor behavior, since mapping the distance between each measured point and the reference line helps verify if the uncertainty is uniform across the entire laser line or if some areas of the sample respond differently. This spatial analysis is necessary to confirm that the linear model correctly represents the block's geometry and to rule out any hidden systematic distortions that the numbers alone might miss.

The following graph shows these fitting residuals, representing the difference between the measured height and the theoretical height defined by the regression line for every point along the scan axis.

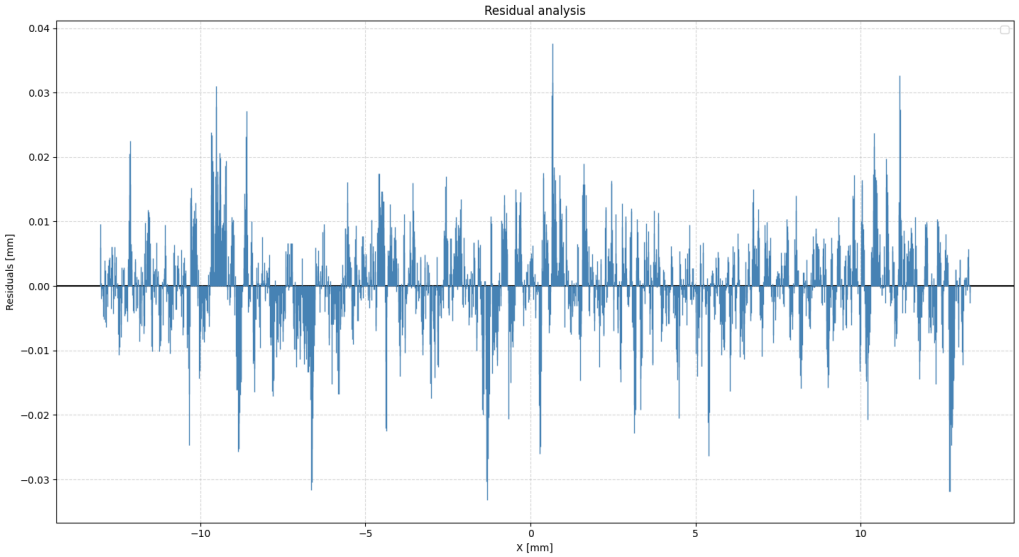

Figure 4.8: Distribution of fitting residuals for the 10 mm gauge block.

The residual plot reveals a few key features of the measurement system: first, the residuals are evenly distributed around the zero axis, which acts as the ideal reference model. The lack of obvious trends, such as curved patterns, periodic oscillations, or leftover slopes, confirms that the linear fit accurately describes the overall geometry of the block, meaning that the mechanical stabilization successfully removed any large systematic drifts.

The observed noise shows rapid, irregular fluctuations typical of high-frequency disturbances, suggesting that the dispersion does not come from geometric defects on the sample or structural movements, but is instead likely caused by the

sensor's internal electronic noise and minor optical variations during the triangulation process. The amplitude of these deviations is well controlled, with most residuals staying within a range of ±0.02 mm. The high density of points around zero matches the previously calculated standard deviation ($\sigma \approx 7.7\,\mu$m), and since almost all residuals fall within a $\pm 3\sigma$ interval, the data confirms a noise distribution close to a normal (Gaussian) one, proving the overall statistical reliability of the scan.

The spatial analysis confirmed that there are no systematic trends along the profile, meaning the data dispersion is not linked to shape errors or geometric drifts. To check if this uncertainty is purely random, the residual values are plotted in a frequency histogram, converting the raw data into a probability distribution that clearly shows how often a certain measurement error happens in a single frame. The goal is to see if the error follows a predictable statistical model, which is a basic requirement to ensure the reliability of the next processing steps.

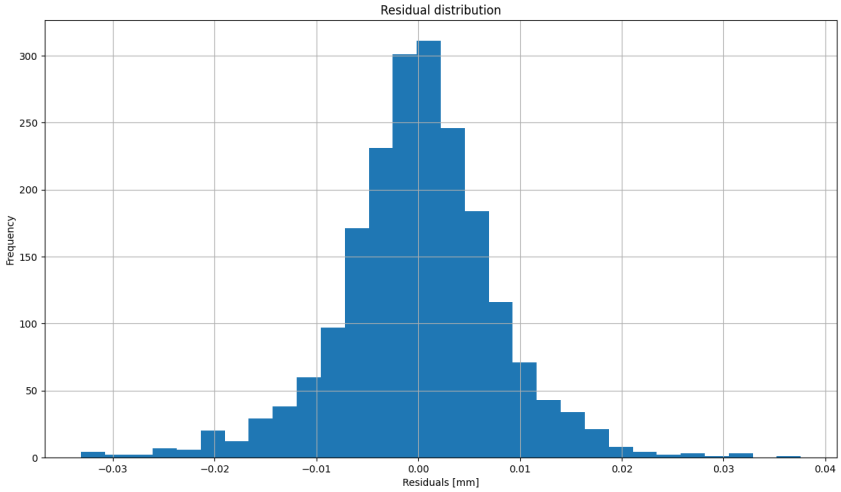

Figure 4.9: Frequency histogram of the fitting residuals.

The graph shows that the data follows a symmetrical bell curve centered at zero, which is typical of a normal (Gaussian) distribution. The narrow, tall shape indicates that most measured points align closely with the ideal line, peaking exactly at zero error, while the rapidly dropping tails confirm that extreme values, or outliers, are statistically rare and have very little impact on the dataset.

This symmetry supports the results from the spatial analysis, confirming that the measurement error is random rather than systematic. Since the data is centered

precisely at zero with no asymmetry, we can conclude that the system is free from underlying biases or recurring mechanical flaws, meaning the deviations are not caused by predictable defects, but by unpredictable variations intrinsic to the measurement process.

This experimental proof is key to validating the measurement method, as a normal distribution with a zero mean identifies the dispersion as white noise, likely coming from the sensor's internal electronics or optical effects like laser speckle. Finally, the lack of asymmetry in the histogram confirms that the mechanical setup does not introduce biased errors, ensuring that any observed deviation comes from the sensor's technological limits rather than structural defects in the support system.

4.2.2 Sensor Limits

Proving that the residual distribution is normal is the basis for applying statistical noise reduction techniques, and since we established that the measurement error is random rather than systematic, we can apply inferential statistics and the Law of Large Numbers to improve the estimation of the physical quantity [37].

The signal captured by the sensor at a specific point can be modeled as a random variable X. Each single measurement x_i is the sum of the true value (μ), which is an unknown constant, and a random error (ϵ_i):

$$x_i = \mu + \epsilon_i \tag{4.5}$$

Following the previous analysis of the residuals, we assume the errors ϵ_i are independent and identically distributed (i.i.d.) random variables. They have an expected value of zero ($E[\epsilon_i] = 0$), which means there is no systematic bias, and a constant variance ($Var(\epsilon_i) = \sigma^2$), which represents the intrinsic noise of a single frame.

Because of this, each individual measurement x_i is also a random variable. Its expected value is equal to the true value ($E[x_i] = E[\mu + \epsilon_i] = \mu + E[\epsilon_i] = \mu$), and its variance is the same as the error's variance, since μ is a constant and the variance of a constant is zero:

$$Var(x_i) = Var(\mu + \epsilon_i) = Var(\mu) + Var(\epsilon_i) = 0 + \sigma^2 = \sigma^2 \tag{4.6}$$

To estimate the true value μ more accurately, we use the arithmetic mean of N consecutive scans. The sample mean $\bar{x}$ is defined as:

$$\bar{x} = \frac{1}{N}\sum_{i=1}^{N} x_i \tag{4.7}$$

First, we check that the sample mean is an unbiased estimator by applying the expected value and using its linearity:

$$E[\bar{x}] = E\left[\frac{1}{N}\sum_{i=1}^{N} x_i\right] = \frac{1}{N}\sum_{i=1}^{N} E[x_i] = \frac{1}{N}\sum_{i=1}^{N} \mu = \frac{1}{N}(N\mu) = \mu \tag{4.8}$$

Since $E[\bar{x}] = \mu$, the average of the measurements will converge exactly to the true value as N increases.

The main goal is to show mathematically how the variance of this new estimator is much lower than the variance of a single measurement. Applying the variance to the sample mean gives:

$$Var(\bar{x}) = Var\left(\frac{1}{N}\sum_{i=1}^{N} x_i\right) \tag{4.9}$$

According to the properties of variance, a constant can be taken out by squaring it ($Var(kX) = k^2 Var(X)$). In our case, the constant is $1/N$:

$$Var(\bar{x}) = \frac{1}{N^2} Var\left(\sum_{i=1}^{N} x_i\right) \tag{4.10}$$

Next, we need to calculate the variance of the sum of these random variables. Generally, the variance of a sum equals the sum of the individual variances plus twice the sum of the covariances between all possible pairs:

$$Var\left(\sum_{i=1}^{N} x_i\right) = \sum_{i=1}^{N} Var(x_i) + 2 \sum_{1 \le i < j \le N} Cov(x_i, x_j) \tag{4.11}$$

At this point, our earlier assumption about independent measurements becomes key. Statistical independence between two scans x_i and x_j (for $i \neq j$) means they are not correlated, so their covariance is zero ($Cov(x_i, x_j) = 0$). As a result, the mixed term in the previous equation disappears, which greatly simplifies the expression:

$$Var\left(\sum_{i=1}^{N} x_i\right) = \sum_{i=1}^{N} Var(x_i) \tag{4.12}$$

Putting this result back into the variance equation for the sample mean, and remembering that each single measurement has a variance of $Var(x_i) = \sigma^2$, we get:

$$Var(\bar{x}) = \frac{1}{N^2} \sum_{i=1}^{N} \sigma^2 \tag{4.13}$$

Since the constant σ^2 is added N times, the sum becomes $N\sigma^2$:

$$Var(\bar{x}) = \frac{1}{N^2}(N\sigma^2) = \frac{\sigma^2}{N} \tag{4.14}$$

This mathematical result has a direct practical effect on the measurement system: the uncertainty of the mean, usually called the Standard Error of the Mean (SEM), drops non-linearly, following the square root of the number of scans:

$$SEM = \sqrt{Var(\bar{x})} = \frac{\sigma}{\sqrt{N}} \tag{4.15}$$

To verify the noise reduction strategy in practice, a detailed analysis was performed on a 10 mm Johnson gauge block to compare the error parameters between 10 consecutive single frames and the averaged profile. The table below summarizes the Mean Absolute Error (MAE), the Root Mean Square Error (RMSE), and the standard deviation of the residuals (σ) for each scan and for the final averaged profile.

Acquisition	**MAE [mm]**	**RMSE [mm]**	**σ residuals [mm]**
Frame 1	0.005712	0.007778	0.007780
Frame 2	0.005710	0.007777	0.007779
Frame 3	0.005708	0.007775	0.007777
Frame 4	0.005715	0.007780	0.007782
Frame 5	0.005711	0.007778	0.007780
Frame 6	0.005709	0.007776	0.007778
Frame 7	0.005713	0.007779	0.007781
Frame 8	0.005710	0.007777	0.007779
Frame 9	0.005714	0.007781	0.007783
Frame 10	0.005712	0.007778	0.007780
Averaged Profile	**0.005691**	**0.007767**	**0.007769**

Table 4.1: Error parameters for single frames and the averaged profile.

Looking at the data reveals a counterintuitive result: the standard deviation of the averaged profile ($\sigma \approx 7.7$ µm) is almost identical to that of the single frames. Even though we would expect the random error to decrease by a factor of $\sqrt{N}$ according to the Law of Large Numbers expressed in eq. (4.15), this does not mean the method failed; rather, it shows that the point dispersion is not caused by random temporal factors like electronic noise or environmental vibrations. Instead, the system seems to be limited by a spatial systematic error that stays "frozen" across every scan. This $7.7\mu m$ deviation is likely due to intrinsic resolution limits or constant optical effects on the surface, specifically laser speckle, which temporal averaging cannot eliminate.

To further validate the measurement process and isolate the sensor's performance from potential disturbances caused by the support structure, a temporal repeatability analysis was done. While the MAE and RMSE describe the spatial dispersion, meaning how far the points are from the fitted line, this repeatability study measures the temporal stability, evaluating how much a specific spatial point fluctuates across the 10 static scans. The statistical analysis gave the following results:

- Average temporal standard deviation (σ_t): $0.00063\mu m$
- Minimum temporal standard deviation (σ_{min}): $0.00021\mu m$

The fact that this temporal deviation remains well below 1 µm (an order of magnitude smaller than the previously calculated fitting error of 7.7 µm) leads to two main conclusions about the study's validity. First, it validates the mechanical setup, as the support structure provides high stability despite being a non-industrial prototype, allowing the sensor to operate at its nominal limits without interference from vibrations or structural bending. Second, this difference explains the actual nature of the error: since each measured point stays effectively locked in its position with almost no variation between frames, the 7.7 µm deviation is confirmed to be a systematic spatial pattern, which is likely an intrinsic characteristic of the sensor, the surface interaction, or laser speckle, rather than a random disturbance that could be reduced through further averaging.

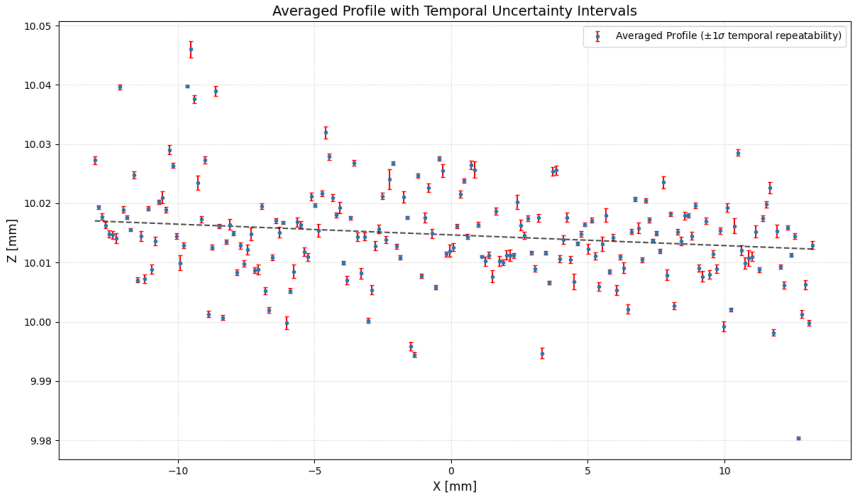

Figure 4.10: Averaged profile plot with temporal error bars showing systematic outliers.

Looking at the averaged profile plot with temporal error bars, we can see that several points look like outliers compared to the linear best-fit trend. While in a purely stochastic system we would expect these points to either move toward the fit line after temporal averaging or at least show much larger error bars due to their random nature, the plot clearly shows that even these apparent outliers have very small temporal standard deviations (σ), similar to the points lying directly on the fit line. This visual evidence confirms that these points are not random measurement errors or temporary noise, but are instead locked in their displaced positions across all 10 scans.

This leads to a clear metrological conclusion: the dispersion seen in the MAE and

RMSE values does not come from temporal instability but is a systematic spatial error. Whether due to the sensor's intrinsic resolution limits or laser speckle effects on the gauge surface, the instrument has reached its intrinsic noise floor, and the stability of these outliers proves that more temporal averaging would not help reduce the residual error, since the measurement has already reached its maximum possible precision for this specific hardware-surface interaction.

To ensure the results were valid and consistent, the whole experimental procedure was repeated under the same conditions on gauge blocks of different sizes, specifically 1 mm, 2 mm, and 5 mm. This comparison has two main goals: first, to check if the noise floor and the error metrics (MAE and RMSE) stay constant across different measurement scales, and second, to confirm that the high temporal stability and the systematic spatial error are standard features of the system rather than just random effects on a single block.

Gauge Block	**MAE [mm]**	**RMSE [mm]**	$\sigma_{spatial}$ **[mm]**	$\sigma_{temporal}$ **[mm]**
1 mm	0.004317	0.005885	0.005887	0.001031
2 mm	0.007101	0.009878	0.009880	0.000887
5 mm	0.003920	0.005024	0.005025	0.000566
10 mm	0.005691	0.007767	0.007769	0.000630

Table 4.2: Summary of error metrics and standard deviations for all analysed gauge blocks.

Comparing the different gauge blocks (1, 2, 5, and 10 mm) gives a clear picture of the instrument's performance. The results are consistent and lead to the following conclusions:

- Identification of the instrument's noise floor: The data show that the spatial error (RMSE and $\sigma_{spatial}$) stays between 5 µm and 10 µm regardless of the block size, which confirms the sensor's intrinsic resolution limit, or noise floor. Since this error does not drop with temporal averaging, it is confirmed to be a systematic spatial pattern likely caused by the sensor's hardware and laser-surface interactions, such as speckle.
- Isolation of sensor performance: The very low temporal standard deviation ($\sigma_{temporal} < 1$ µm) is key to validating the instrument, because by proving that the test setup introduces almost no vibration or mechanical drift, we

can conclude that the spatial dispersion comes entirely from the sensor itself. This shows that the instrument is working at its maximum stability and that the measured deviations represent its true internal uncertainty.

- Reliability across the measuring range: Since the error metrics do not depend on the size of the gauge block, the sensor's response is uniform across different parts of its measuring range, meaning the instrument has a stable uncertainty profile and proving it is a reliable tool for high-precision profile reconstruction.

4.3 Sensor-tool interaction analysis

After testing the sensor with the gauge blocks, the next step was to study how the laser interacts with the actual tool, since it is also important to evaluate how the specific surface finish and the curved geometry of the end mill affect the data quality. To perform a proper analysis using a known geometric reference, we first focused on the tool shank, which, unlike the cutting edges that have complex geometries from material removal processes, keeps the original cylindrical shape of the blank.

Using the shank as a reference model offers great metrological advantages because, geometrically, a perfect cylinder cut by a perpendicular plane produces a perfectly circular profile, which is easy to analyse. Furthermore, the shank serves as a perfect natural standard because it is ground with very high precision to avoid the manufacturing uncertainties and sharpening tolerances typical of cutting edges, allowing us to test the sensor's response on reflective metallic surfaces without unknown shape errors interfering with the results.

The goal of this phase is to use the same analysis method applied to the gauge blocks, specifically through fitting and residual analysis. By replacing the linear model with a circular fit, we can measure how well the Gocator sensor reconstructs the tool's curvature by directly comparing the acquired point cloud against the ideal circle that acts as the reference for this cylindrical section.

4.3.1 Optical Reflections and Signal Saturation

Extracting the circular profile of the tool shank presents a practical optical issue due to the target's material, as the polished metal and cylindrical shape of the tool make its interaction with the laser beam quite complex. Specifically, at the top of the cylinder, the metallic surface acts like a mirror rather than scattering the light evenly, reflecting the incident laser light straight back into the sensor lenses. As a result, this specular reflection concentrates a large amount of optical energy onto a small group of pixels in the camera matrix, causing local saturation.

To understand how this localized energy affects measurement accuracy, we need to look at how the profiler processes the raw optical signal. To convert the pixel image from the CMOS sensor into a precise vertical coordinate, the system does not just pick the brightest pixel; instead, it relies on a center of mass calculation [38], usually called a centroid algorithm, which is applied independently to each vertical column of the sensor.

In ideal scanning conditions, the light intensity profile of the laser line distributed along a vertical column follows a Gaussian or bell-shaped curve. This continuous distribution occurs because the laser beam possesses a physical thickness, and the reflected light naturally scatters across a small group of adjacent photodiodes, illuminating them at varying intensity levels. To determine the exact geometric center of this laser line, the algorithm calculates a weighted average by taking the discrete vertical positions of the illuminated pixels Z_i and weighing them according to their corresponding light intensities I_i. The theoretical center of the laser profile is computed using the following mathematical formulation:

$$Z_{subpixel} = \frac{\sum(Z_i \cdot I_i)}{\sum I_i} \tag{4.16}$$

By interpolating the intensity data, this peak detection algorithm finds the theoretical maximum of the light curve, overcoming the physical grid limits of the sensor and allowing the profiler to reach a highly accurate subpixel resolution, which is key to the system's performance.

However, since this subpixel precision depends entirely on evaluating the intensity variations between adjacent pixels to find the true center of the Gaussian curve, any optical saturation disrupts the mathematical process. When the specular reflection from the top of the metallic cylinder overexposes the sensor, the affected photodiodes simply hit their maximum capacity, causing the peak of the bell curve to flatten out or clip and resulting in a loss of information. Without the

necessary intensity gradients, the algorithm cannot find the true peak, which shifts the calculated coordinates away from the actual cylindrical profile.

To see how the centroid algorithm behaves under these extreme lighting conditions, it helps to look at the raw pixel data, as the following figures show the laser profile reflected from the metallic tool by comparing an optimal exposure with a heavily saturated one.

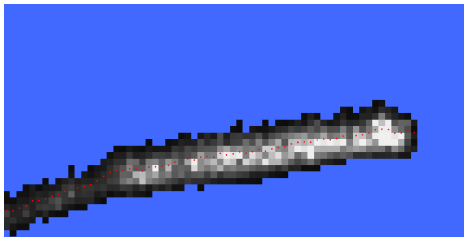

(a) Optimal exposure with a well-defined intensity peak.

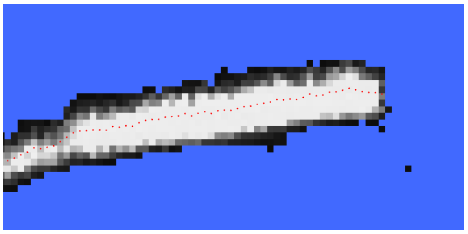

(b) Saturated profile due to prolonged exposure.

Figure 4.11: Sensor's field of view on a cutting edge at different exposure times.

Figure fig. 4.11a shows an optimal exposure where the light intensity profile is well defined without reaching the sensor's maximum capacity, preserving the Gaussian curve and allowing the algorithm to smoothly interpolate the peak. In contrast, Figure fig. 4.11b shows the heavily saturated scan caused by the mirror effect, where a large cluster of pixels is completely whited out, visually flattening the theoretical peak and reducing the local intensity gradient.

Even though the calculated subpixel points might look almost identical in a single scan, saturation ruins the long-term measurement repeatability because, in an overexposed condition, the centroid calculation is forced to rely only on the few non-saturated pixels left at the edges of the flattened peak. Since these outer pixels have a very low light intensity, they are highly sensitive to optical noise and temporal fluctuations, meaning their values can vary a lot from one scan to another, noticeably increasing the statistical dispersion of the measurement.

On the other hand, an optimal exposure setting not only captures the true maximum of the bell curve but also provides more valid intensity values along the Gaussian slopes. Relying on this better-distributed data gives a stronger mathematical foundation for the interpolation algorithm, which improves the system's repeatability and reduces the overall margin of error. The practical effect of this geometric distortion will become clear in the next residual analysis, where a peak

of systematic deviation perfectly matches the spatial coordinates of the saturated top of the cylinder.

4.3.2 Circle Fitting and Radius Estimation

After analysing the physical problem of optical saturation in the previous section, the next step is to measure how these local reflection issues affect the overall measurement quality by directly comparing the acquired point cloud of the metallic tool shank against its ideal reference shape.

To estimate the geometric parameters of the circular profile a nonlinear least squares fitting algorithm is employed. Let the set of N acquired data points be defined as (x_i, z_i) for $i = 1, \ldots, N$. The standard algebraic equation of a circle with center (x_c, z_c) and radius r is given by the following expression:

$$(x - x_c)^2 + (z - z_c)^2 = r^2 \tag{4.17}$$

To find the best parameters, an optimization problem is set up to minimize the geometric distance between the data points and the estimated circle, where the residual d_i for each data point is defined as the orthogonal distance from the point to the perimeter of the theoretical circle:

$$d_i = \sqrt{(x_i - x_c)^2 + (z_i - z_c)^2} - r \tag{4.18}$$

The main goal of the least squares algorithm is to find the set of parameters (x_c, z_c, r) that minimizes the sum of the squared residuals $\sum_{i=1}^{N} d_i^2$. Since this residual function is strictly nonlinear with respect to the center coordinates, an iterative solver is needed to reach convergence, which requires starting with a reasonable initial guess. Therefore, the initial center coordinates (x_0, z_0) are calculated using the mean of the spatial data, while the initial radius r_0 is approximated using half the vertical range of the dataset.

The implementation of this numerical approach, based on `scipy.optimize` library, is presented in listing 4.2.

Once the iterative algorithm converges to the optimal parameters (x_c, z_c, r), the fitted curve can be reconstructed by solving the circle equation for the vertical coordinate z, which is given by the following expression:

$$z = z_c \pm \sqrt{r^2 - (x - x_c)^2} \tag{4.19}$$

Listing 4.2: Non-linear least squares circle fitting algorithm.

```
from scipy.optimize import least_squares
import numpy as np

def circle_residuals(params, x, z):
    xc, zc, r = params
    return np.sqrt((x - xc)**2 + (z - zc)**2) - r

# Initial estimation
x0 = np.mean(x)
z0 = np.mean(z)
r0 = (np.max(z) - np.min(z)) / 2
initial_guess = [x0, z0, r0]

# Fitting process
result = least_squares(circle_residuals, initial_guess, args=(x, z))
xc, zc, r = result.x

# Reconstructing the fitted curve
theta = np.linspace(np.min(x), np.max(x), 500)
z_fit = zc + np.sqrt(np.clip(r**2 - (theta - xc)**2, 0, None))
```

To reconstruct the upper profile of the tool shank, the standard circle equation is solved for z, and since the optical sensor scans the metallic cylinder from above, only the top half of the profile is captured during the test. Therefore, only the positive branch of the solution is used to isolate the surface of interest, allowing for a precise comparison between the theoretical model and the real point cloud.

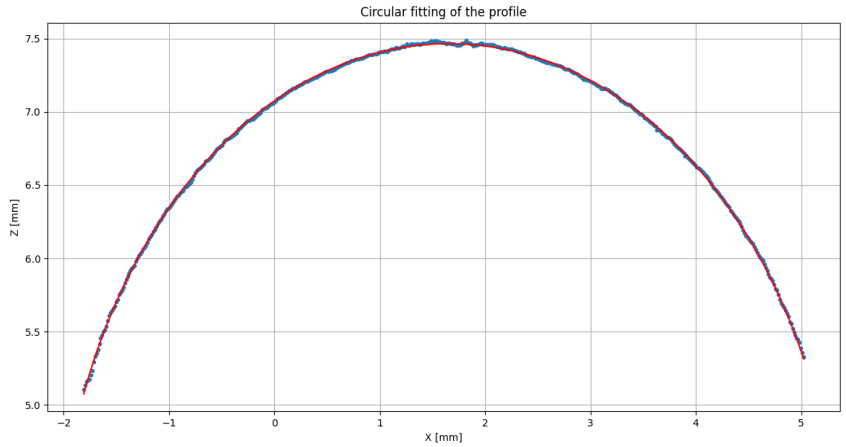

Figure 4.12: Circle fitting applied to the tool shank and corresponding residual distribution.

As shown in fig. 4.12, the points detected by the sensor in the upper part of the cylinder deviate significantly from the ideal circumference, and the magnitude of this anomaly can be quantified looking at the residual graph, which displays a clear peak of systematic deviation exactly at the top of the cylinder.

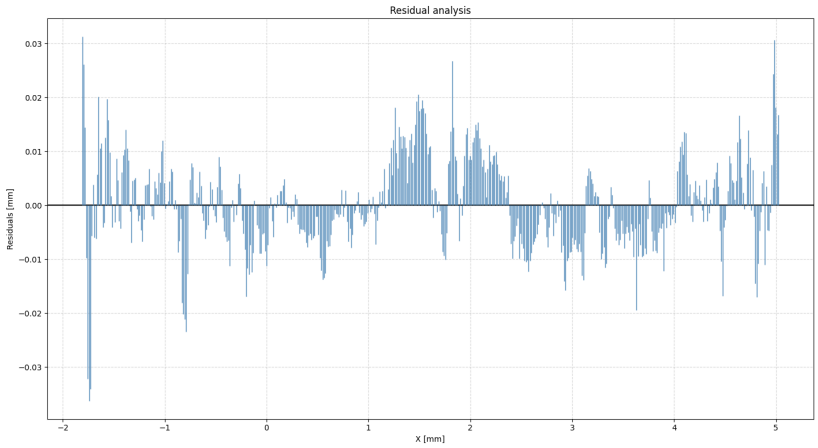

Figure 4.13: Quantitative residual analysis detailing the systematic deviations of the circular profile.

This localized geometric distortion perfectly confirms the optical limitations analysed in section 4.3.1, as the local curvature at the top of the tool shank causes the laser beam to reflect almost entirely back into the sensor lenses, triggering local saturation. Because of this overexposure, the light intensity profile is flattened, which causes the centroid algorithm to fail in calculating the correct subpixel coordinates and ultimately shifts the acquired points away from the actual geometric profile of the metallic piece.

After analysing these physical limitations and geometric distortions, the focus shifts to the metrological reliability of the mathematical fitting. To rigorously evaluate the dimensional accuracy and repeatability of this method, a measurement campaign was carried out on five different industrial tools by repeatedly applying the circular fitting algorithm across multiple consecutive scans. This allowed us to extract both the estimated radius and its standard deviation to provide a direct measure of the system's stability. These values were then compared against the nominal dimensions dictated by standard manufacturing specifications, and the complete results of this experimental phase are detailed in table 4.3, offering an objective assessment of the sensor's overall performance under real operating conditions.

Instrument	**Radius [mm]**	**Sigma (σ) [mm]**	**Target [mm]**
Tool 1	2.9975	0.0005	3.00
Tool 2	3.7101	0.0003	3.75
Tool 3	5.9780	0.0005	6.00
Tool 4	4.9864	0.0005	5.00
Tool 5	2.9983	0.0005	3.00

Table 4.3: Comparison of fitted radii standard deviations and nominal values.

The experimental results shown in table 4.3 confirm the reliability of the developed optical system, as the key metric (the standard deviation) stays well below one micrometer for all the tested tools. This proves the submicron repeatability of the scanning procedure, showing that both the sensor and the nonlinear fitting algorithm produce highly stable results across multiple consecutive scans.

Furthermore, comparing the estimated radii with the nominal values reveals a high degree of dimensional accuracy. While the measured values show a slight but consistent negative deviation from the nominal targets, this is not a measurement error; instead, this slight undersizing perfectly matches the strict manufacturing tolerances applied to industrial tool shanks, which are intentionally ground to a slightly smaller diameter to ensure a secure fit inside the machine spindle. Ultimately, these results validate the methodology by confirming that the final measurements remain highly stable and accurate despite the optical issues and geometric distortions discussed earlier.

4.4 Geometric Occlusions

As introduced in section 3.1, laser triangulation suffers from physical occlusion, and looking at the tool geometry in fig. 2.2, it is clear how some structural features, like a negative rake angle, fall completely outside the optical line of sight, since the tool body blocks the incident laser beam or the reflected signal, making these undercut surfaces impossible to measure during a standard static scan.

To overcome this limitation, a laboratory test was done by placing the piece in controlled rotation, with the results shown in fig. 4.14, where two different angular positions of the same cutting edge are captured. While the surface remains completely hidden in the optical shadow in the first position, rotating the tool around its main axis brings it out of the shadow, making it fully visible and measurable by the sensor.

This dynamic approach creates an efficient measurement method, because by taking a reference position (which corresponds to the standard measurement angle) and then rotating the piece by a known angular offset, the previously hidden geometries can be exposed to the laser.

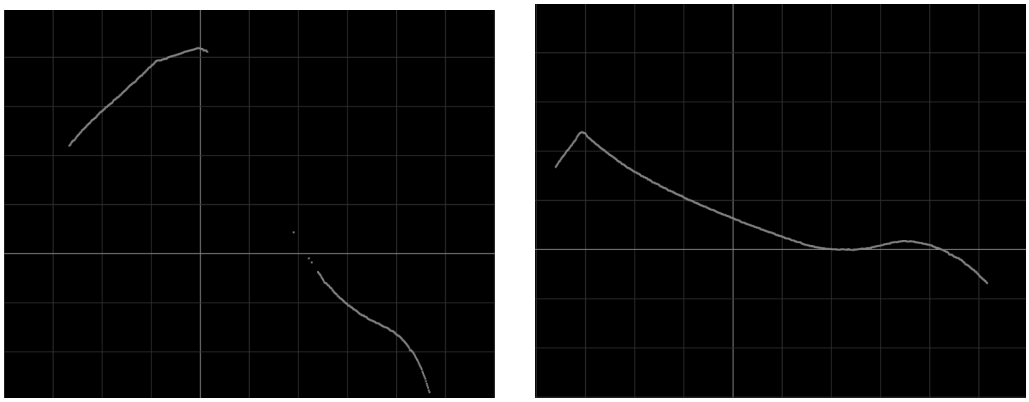

(a) Cutting edge in the shadow zone **(b)** Cutting edge visible after rotation

Figure 4.14: Visual comparison of the same cutting edge before and after the applied angular rotation.

Importantly, this solution provides a major hardware advantage, as using a single triangulation unit combined with precise part rotation eliminates the need for complex multi-laser setups like the one seen in fig. 3.2. Traditionally, overcoming severe optical occlusions requires surrounding the tool with multiple sensors, which greatly increases the hardware cost, the physical footprint of the measuring

station, and the computational effort needed to align overlapping point clouds. By avoiding this extra hardware, the proposed single-sensor architecture remains simple and cost-effective.

While successfully validated in the lab, this rotational measurement procedure will be fully automated once the optical device is installed on the industrial Speroni machine, which natively guarantees precise control of the spindle rotation.

Chapter 5

System Integration

Following the theoretical study of 3D optical technologies and the experimental results obtained with the laser triangulation sensor, Speroni validated the potential of this device, confirming its suitability for the geometric analysis of cutting edges and its integration into their presetting systems. In order to conduct field tests on the dedicated Speroni machine (shown in section 2.2), the physical installation of the optical device was achieved through a custom adapter plate, designed and manufactured in close collaboration with the company's technical team to ensure a stable and robust mechanical coupling to the moving structure, which can be seen in fig. 5.1.

During this phase, the research focused on validating measurement quality and developing the profile analysis software, rather than delivering a commercial prototype. Therefore, the real-time integration between the developed code and Speroni's proprietary numerical control (CNC) was left to future developments. The system currently operates with a decoupled software architecture: the machine's advanced kinematics are used to position the optical device with absolute precision, while the sensor independently performs the scan. The raw profiles are then exported as .csv files and processed offline within a custom-developed application. This decoupled approach successfully isolated the metrological challenge, allowing the research to focus only on validating and optimizing the mathematical algorithms required to extract, correct, and stabilize the angular data.

Figure 5.1: Laser triangulation sensor mounted on the Speroni machine.

This chapter details the software development process, providing a comprehensive analysis of the specific metrological challenges associated with this type of optical measurement and the strategies used to solve them. Rather than just outlining the code, the text explaines the practical problems encountered during the testing phase, such as the necessity of defining an absolute angular reference frame and the critical measurement inconsistencies arising from raw data extraction.

By examining these issues, the chapter explains how the developed methodologies, from a kinematic alignment logic to a robust iterative fitting algorithm, were specifically designed to filter the data, correct inaccuracies, and give the user precise control over both the measurement process. Finally, the effectiveness of these solutions is demonstrated through an experimental validation campaign conducted on various industrial cutting tools.

5.1 System Alignment

The main goal of the measurement system is to determine the geometric parameters of the tool discussed in section 2.1, focusing on the clearance and rake angles. However, as analyzed in section 4.4, laser triangulation is affected by intrinsic limitations related to its optical nature: the complex shape of the cutting edge and the orientation of its surfaces create optical occlusions, preventing the direct acquisition of the rake angle and the analysis of the clearance angles within a single scan.

To overcome this limitation, a kinematic alignment strategy has been implemented to establish an absolute reference position, corresponding to the theoretical configuration illustrated in fig. 2.2. By recording this position, the exact value of any subsequent rotation is known, allowing the system to orient the sensor at the optimal scanning angle for each specific face, minimizing occlusions and maximizing surface visibility.

The first step in the alignment procedure is to center the tool's axis of rotation with the sensor's central axis. This preliminary alignment greatly simplifies the subsequent definition of the zero reference configuration, since moving the machine to a position where the cutting edge tip lies directly on this axis ensures that the radial line connecting the tip to the center is perfectly vertical, allowing for a straightforward verification of the correct setup. As previously demonstrated in chapter 4, the center of rotation can be obtained by analyzing the unmachined tool shank, whose perfectly circular cross-section allows its geometric center coordinates to be extracted by fitting a circle to the acquired profile.

While the algorithm explained in section 4.3.2 could be applied for this task, it's implementation would be highly inefficient during the setup phase. Given the decoupled architecture of the system, the operator would need to repeatedly export raw data for offline processing during each alignment operation. Instead, to ensure an efficient and practical workflow, this preparatory stage uses the sensor's built-in smart camera tools, which can perform real-time circle fitting directly on the hardware, providing the immediate feedback loop necessary for rapid and interactive axis centering, as demonstrated in fig. 5.2.

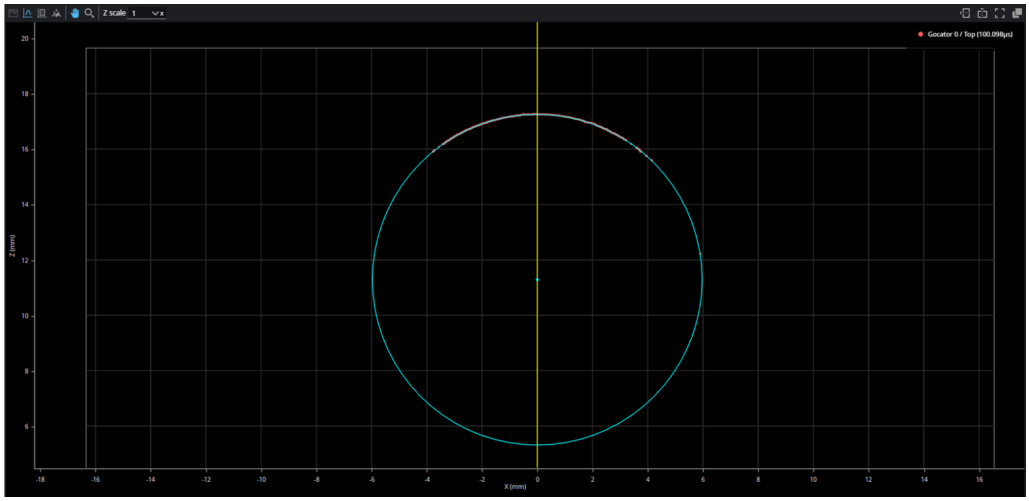

Figure 5.2: Real-time circle fitting on the tool shank.

Once the axis is centered on the shank, the machine translates vertically to the cutting portion of the tool, where the operator visually aligns the cutting edge tip with the rotation axis (fig. 5.3). Although this phase is performed manually, its impact on measurement uncertainty is minimal: according to Speroni's specialists, the angular error resulting from visual alignment is limited to a few hundredths of a degree. Consequently, such a deviation is considered negligible relative to the tolerances typically required for industrial tool presetting.

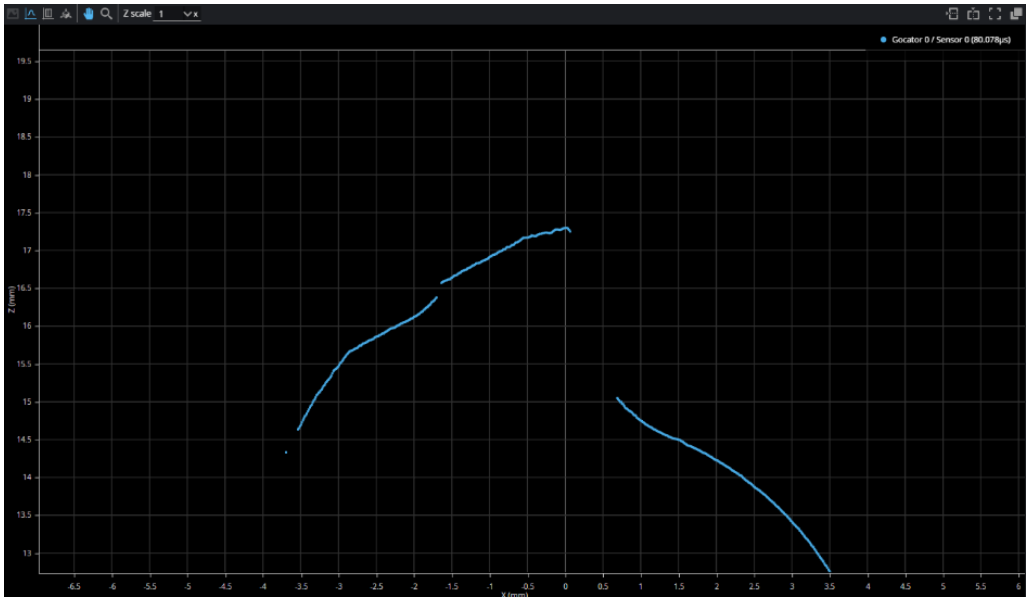

Figure 5.3: Visual alignment of the tool tip with the rotation axis.

Once this configuration is achieved, the angular position is set to zero using the Speroni machine's software. By defining this zero point directly on the cutting edge tip, the machine can rotate the tool to find the best scanning angles and avoid occlusions. During these rotations, the machine tracks the exact angular displacement, providing a reliable baseline coordinate that is then integrated with the sensor's optical readings. This is achieved through a kinematic formula used to compute the final absolute angle (α_{final}):

$$\alpha_{final} = 360^\circ - \theta_{CNC} + \theta_{mesaured} \tag{5.1}$$

where θ_{CNC} is the angular displacement recorded by the machine relative to the zero-reference, and $\theta_{measured}$ is the local angular value extracted by the software from the scanned profile. This approach ensures that the system can reconstruct the absolute orientation of any tool feature, being able to compensate for the physical rotations required to avoid optical occlusions.

5.2 Data Processing

Once the kinematic alignment had been completed and the absolute angular reference established, the focus shifted to the direct acquisition and geometric analysis of the cutting edge. Once the tool has been rotated into the optimal configuration, the raw optical data must be acquired and processed. To effectively eliminate the random error inherent in optical measurements, the technical requirements specified by Speroni state that all algorithmic calculations must be performed on pre-averaged profiles rather than on individual raw scans. To meet this requirement, a specific acquisition strategy was implemented using the sensor's proprietary software.

The optical system was configured in '3D surface analysis' mode, which normally requires setting a known translation step that allows the sensor to position the scanned planes one after the other in the correct position. However, during the scanning phase, the machine's mechanical axes supporting the tool were kept completely stationary. As the sensor operates on the assumption of continuous motion, this procedure repeatedly captures the same XZ cross-section over time, artificially 'stacking' it along the Y-axis. As illustrated in fig. 5.4, the result is a three-dimensional surface composed of multiple identical profiles of the static cutting edge.

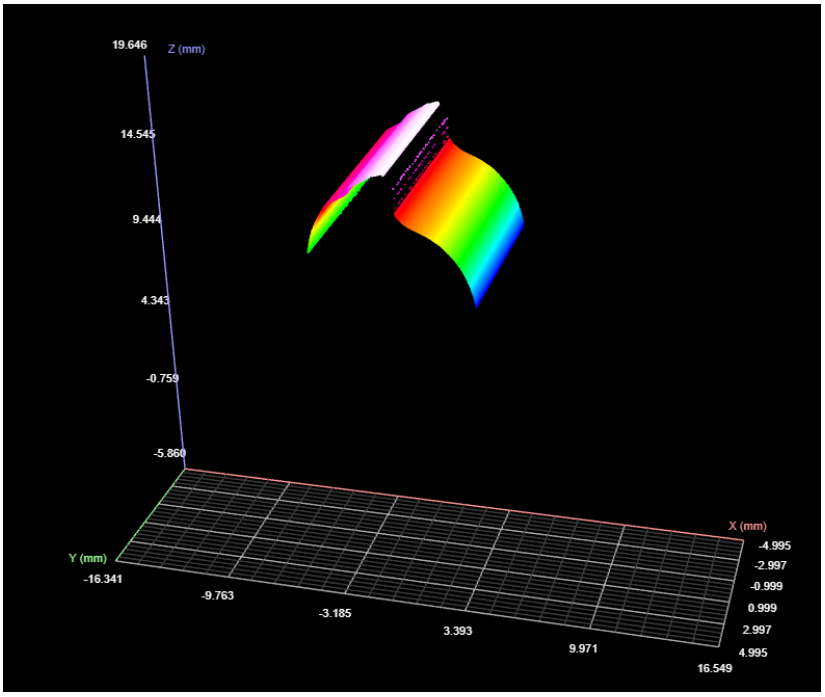

Figure 5.4: 3D surface generated by scanning a stationary tool.

These raw spatial coordinates are exported in .csv format for offline processing. To extract the stable 2D representation required for geometric analysis, a spatial averaging operation is performed on this 3D point cloud: for each discrete X-coordinate, the corresponding Z-values distributed along the Y-axis are averaged, effectively filtering out random optical scattering and localised micro-irregularities, condensing the data into a single 2D average profile. In this context, a single exported .csv file represents a complete acquisition sequence, defined as a 'frame'.

Furthermore, to meet the rigorous validation standards required, the analysis of a single frame is considered insufficient for a reliable metrological evaluation. The industrial protocol specified by Speroni requires the acquisition of 10 consecutive frames to extract ten distinct angular values, which are then statistically processed, calculating the mean, the measurement range, and the standard deviation (σ), to validate the system's overall reliability and repeatability.

Once the average 2D profiles have been generated for each frame, the next step involves extracting the precise geometric features. Initially, the preliminary linear fitting code discussed in listing 4.1 was applied to the entire dataset, but as illustrated in fig. 5.5, this global approach turned out to be inadequate for analysing the complex micro-geometry of a real cutting tool.

The algorithm attempts to evaluate the profile indiscriminately, as it did with the reference blocks, failing to distinguish between the segment to be analysed and the surrounding micro-irregularities or curvatures of the cutting edge. Consequently, this unconstrained fitting misaligns the reference line, producing incorrect angular measurements.

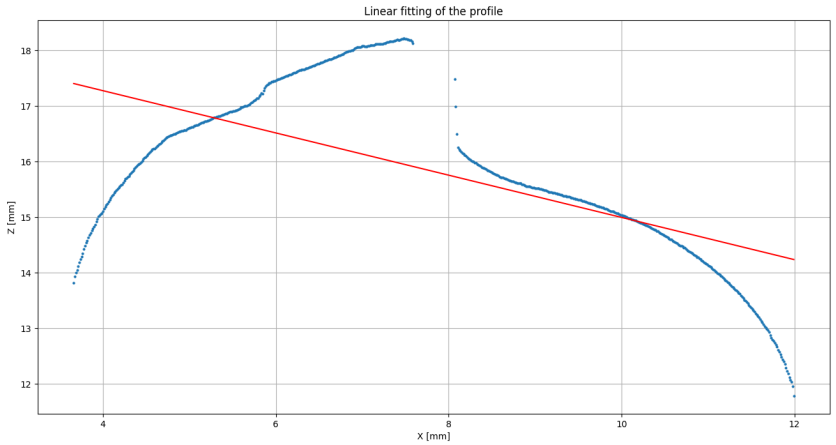

Figure 5.5: Erroneous angular measurement resulting from a global profile analysis.

The limitations highlighted above made it necessary to adopt a targeted data extraction strategy: since the section of the cutting edge to be analysed occupies only a portion of the entire scanned profile, it became essential to isolate the specific points according to the operator's requirements.

To achieve this, a customised graphical user interface (GUI) was developed. Upon launch, the software automatically overlayes a predefined, interactive Region of Interest (ROI) onto the plotted profile. Instead of defining a new area from scratch, the operator can visually inspect the data and manually adjust the boundaries of this selection rectangle, by dragging its vertices, to precisely capture the functional segment of the cutting edge.

Computationally, the software extracts the spatial coordinates of the ROI's vertices, generating a boolean mask that filters the dataset, isolating only the spatial coordinates (x_i, z_i) that fall strictly within the defined rectangle ($x_{min} \leq x \leq x_{max}$ and $z_{min} \leq z \leq z_{max}$). Once the subset of points is successfully isolated, the linear fitting algorithm is applied to compute the slope (m) and the corresponding absolute angle (θ).

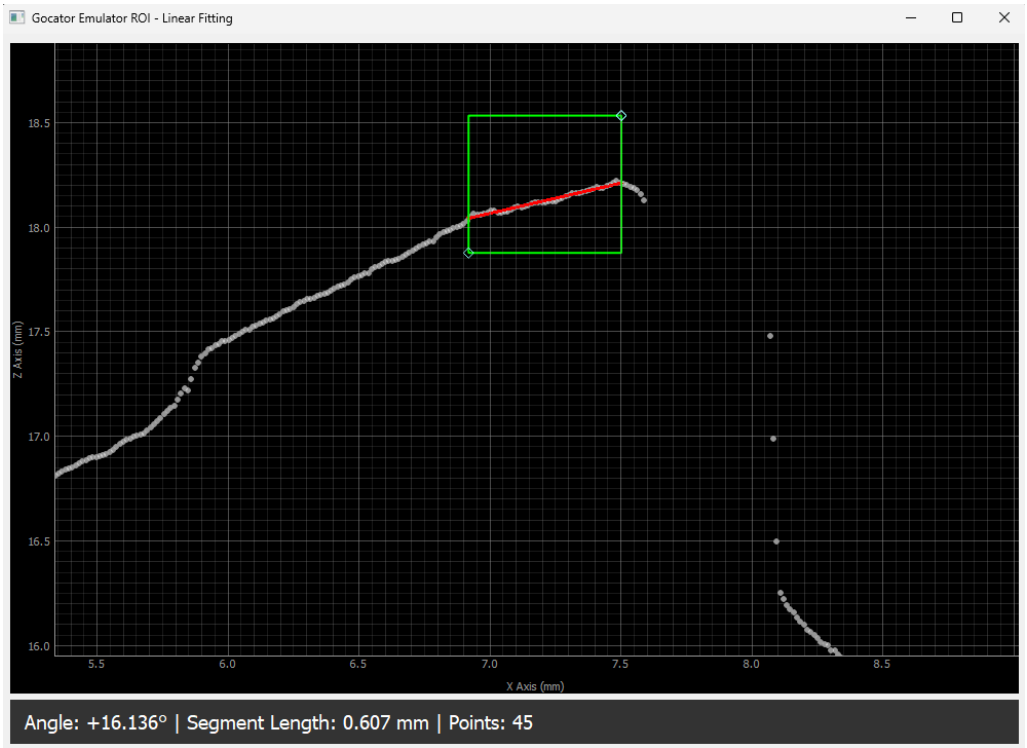

Figure 5.6: Successful angular and length measurement within a manually adjusted ROI.

In addition to angular measurement, the custom GUI has been programmed to simultaneously calculate the spatial length of the analyzed segment. This metric is highly requested in industrial tool presetting, particularly for evaluating clearance and rake angles, as it defines the actual extension of the functional cutting surface. The segment length L is mathematically derived using the horizontal width of the ROI ($\Delta x = x_{max} - x_{min}$) and the previously computed angle θ, according to the following trigonometric relationship:

$$L = \frac{\Delta x}{\cos(\theta)} \tag{5.2}$$

5.3 Algorithmic Stabilization

While the implementation of the manual ROI successfully adapts the evaluation strategy to the specific complexities of cutting tools this approach introduces a new critical variable to the measurement chain: operator dependency.

Since the boundaries of the analysis are defined visually by the user, the final angular value remains intrinsically linked to subjective judgement. Different users may apply different criteria when selecting which points to include, based on their own interpretation of which portion of the profile actually represents the functional cutting edge. As illustrated in fig. 5.7, which displays four different ROI selections on the exact same workpiece, each operator can isolate a different subset of data. The regression algorithm is highly sensitive to these manual variations; the inclusion or exclusion of even a single data point can directly affect the calculated slope, thereby compromising the absolute repeatability required for tool presetting.

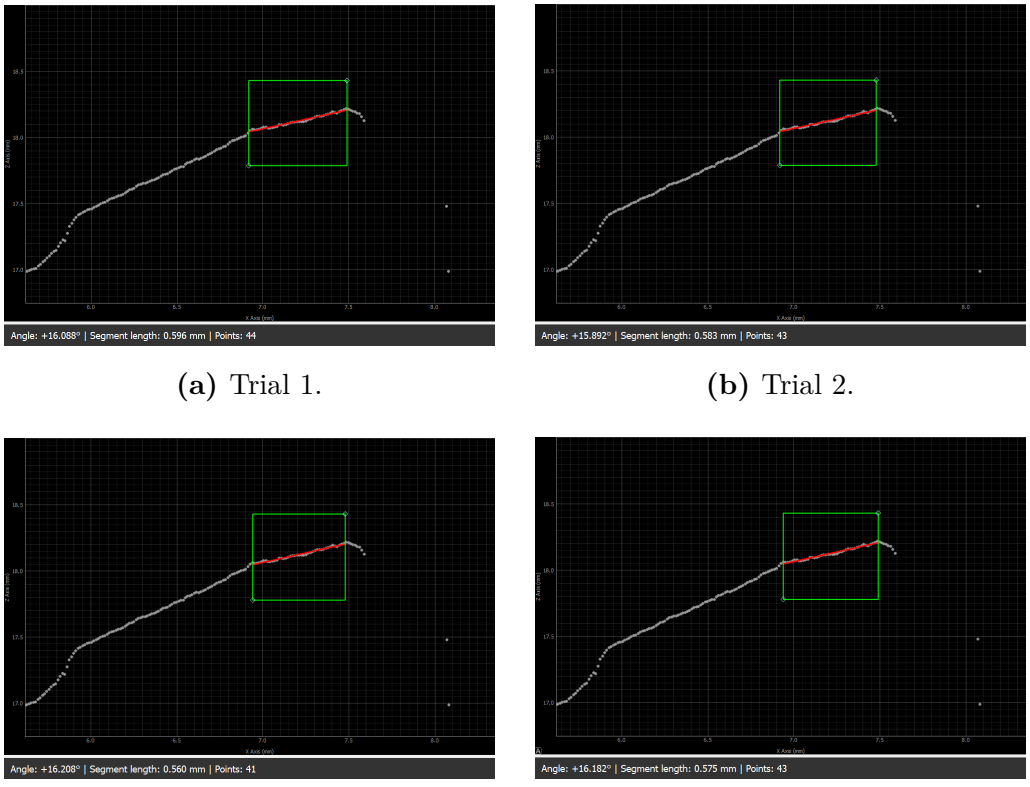

(a) Trial 1. **(b)** Trial 2.

(c) Trial 3. **(d)** Trial 4.

Figure 5.7: Operator dependency in manual ROI selection

Furthermore, the current logic employed to calculate the segment length introduces an additional layer of inconsistency. The length measurement is determined exclusively by the geometric boundaries of the ROI box, rather than the actual spatial coordinates of the laser points captured within it. Consequently, it is possible to obtain varying length values for the exact same set of physical points simply by adjusting the outer limits of the ROI.

To eliminate human variability, it was necessary to introduce a methodology that would ensure measurements were always calculated in a consistent and repeatable manner. The choice fell on the development of an Iterative Robust Fitting algorithm, integrated directly into the software architecture. Starting from a series of points selected by the user, the algorithm is able to autonomously distinguish which points belong to the actual geometric profile and which, on the other hand, should be discarded. In this way, the operator's task is limited only to framing the entire area to be analysed, including any irrelevant points; the algorithm then processes the data set and systematically isolates only the functional cutting edge, eliminating physiological 'outliers' such as residual optical noise, micro-debris or or any change in slope representing another plane of the cutting edge.

To implement autonomous analysis logic and eliminate user dependency, the algorithm does not accept the initial least-squares fit as definitive, but uses it as a basis for identifying which points within the ROI are actually relevant. The core of this automatic selection lies in the error evaluation criterion: instead of considering the classic vertical residuals, which would be geometrically distorted on inclined surfaces such as those of cutting edges, the software calculates the Euclidean distance of each individual point (x_i, z_i) from the estimated line $z = m \cdot x + q$. This perpendicular distance d_i, which represents the actual physical deviation of the point from the ideal profile, is calculated as:

$$d_i = \frac{|m \cdot x_i - z_i + q|}{\sqrt{m^2 + 1}} \tag{5.3}$$

Once the set of orthogonal distances has been obtained, the system identifies the point with the maximum deviation (d_{max}) and compares it with a predefined threshold (for example, 0.010 mm), which defines the maximum acceptable error limit for the profile being analysed.

The core logic of this automatic filtering process is detailed in the Python function `calculate_fit`, which can be found in Appendix A.1. The algorithm operates through a recursive cycle of linear regression, error evaluation and dynamic point removal. The complete operational logic of the developed Batch Analyzer, from initial data acquisition to the final statistical report, is summarised in the flowchart shown in fig. 5.8.

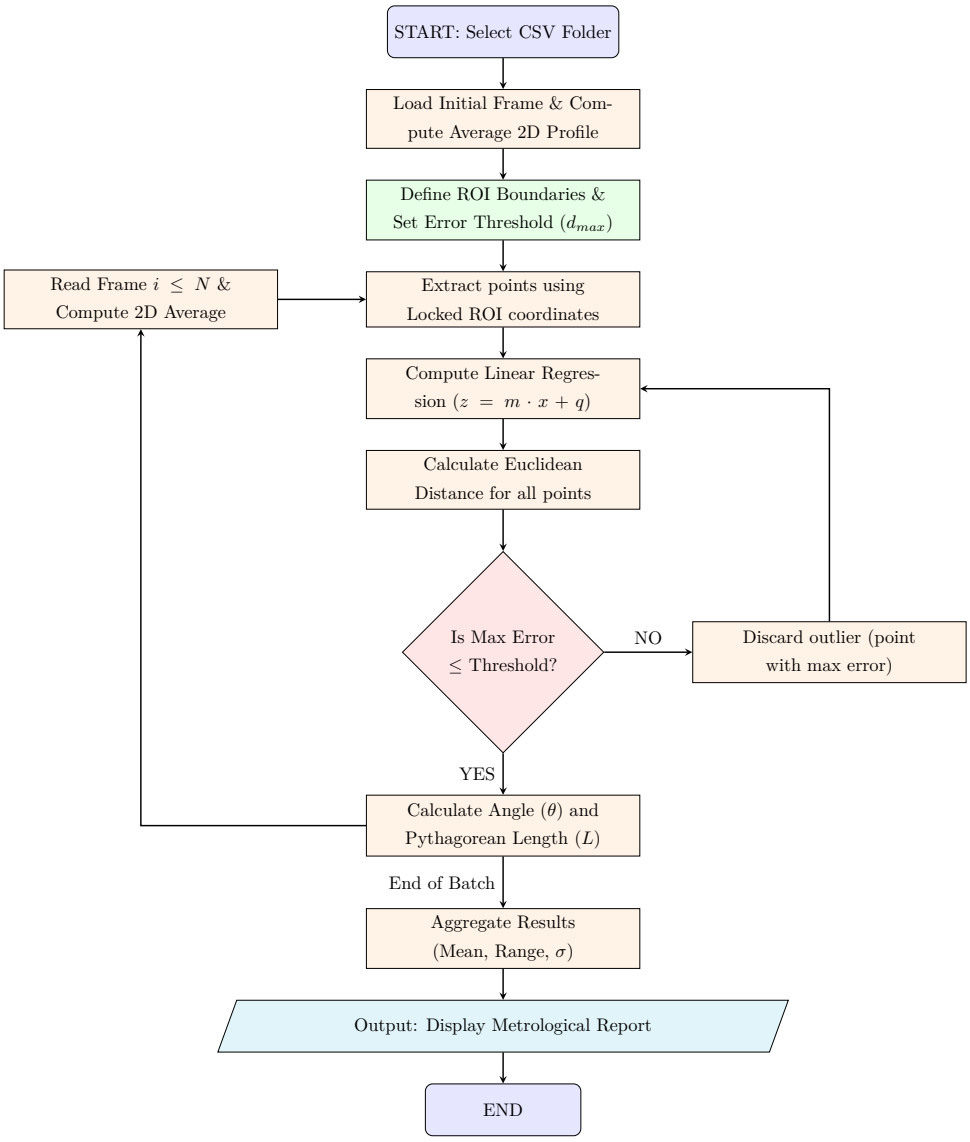

Figure 5.8: Flowchart of the custom Multi-Frame Analyzer logic.

If the value of d_{max} exceeds the threshold, the data point is classified as an outlier and removed from the dataset. Since the exclusion of even a single data point alters the distribution of the data, the previous fit is recalculated and the cycle begins again: the algorithm performs a new regression, calculates the new

distances and identifies the new d_{max}. This process of progressive rejection continues iteratively until all remaining points have a deviation below the threshold. In this way, the algorithm autonomously 'cleans' the operator's selection, ensuring that the final line is calculated exclusively on the inliers (the valid points) of the cutting edge. The result is a consistent and repeatable measurement, which ignores any spurious points erroneously included in the initial ROI.

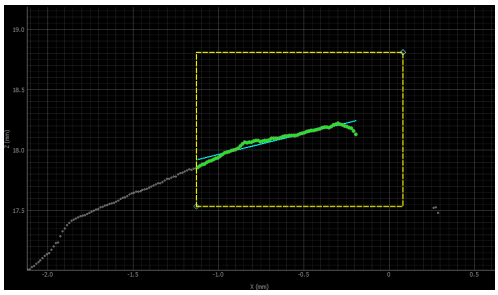

(a) Initial fit affected by noise.

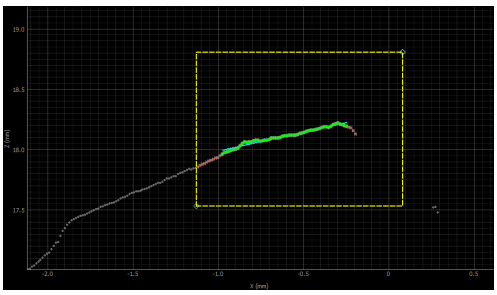

(b) Intermediate outlier rejection.

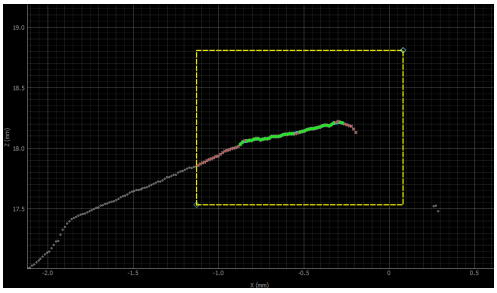

(c) Final stabilized fit.

Figure 5.9: Sequential visualization of the Iterative Robust Fitting algorithm.

The implementation of this iterative logic radically transforms the user experience of the software, shifting the responsibility of accuracy from the operator to the algorithm. The main advantage lies in the simplification of the analysis procedure: the user is only required to roughly frame the area of interest. As illustrated in fig. 5.9, the algorithm is able to autonomously identify the relevant data set, starting from a heterogeneous point cloud (fig. 5.9a), proceeding with the progressive elimination of spurious features (fig. 5.9b), until it isolates exclusively the cutting edge profile (fig. 5.9c).

The robustness of this approach is guaranteed by the nature of the fitting process. As long as the points belonging to the functional geometry constitute the statistical majority within the ROI compared to external outliers (such as background

noise or debris), the regression model will mathematically converge towards the actual profile. This automatic mechanism ensures that, regardless of a slightly imprecise or overly generous manual selection, the final result of the angular analysis remains consistent, ensuring the complete repeatability of the measurement, making it immune to the subjective interpretations of different operators.

The introduction of the selective filtering mechanism also required a modification of the method used to calculate the length of the functional segment. In the standard approach based on manual ROIs, the length was derived trigonometrically using the absolute boundaries of the rectangle drawn by the user. However, since the iterative algorithm actively discards points (often at the outer edges of the ROI where the curvature of the tool tip begins) using the theoretical boundaries of the box would lead to a systematic overestimation of the actual straight-line length of the cutting edge.

To resolve this issue, the software discards the calculation based on the ROI boundaries in favour of a direct spatial measurement, based exclusively on the inliers. Once the iterative cycle has been completed and the stable subset of valid points has been consolidated, the algorithm identifies the actual spatial coordinates of the first (x_{min}, z_{min}) and last (x_{max}, z_{max}) validated points along the line. The actual length of the functional segment L is then calculated as the pure Euclidean distance between these two endpoints:

$$L = \sqrt{(x_{max} - x_{min})^2 + (z_{max} - z_{min})^2} \tag{5.4}$$

By calculating the length exclusively between verified physical points, rather than relying on the theoretical boundaries of the ROI, the software ensures that the reported dimensional measurement accurately represents the effective portion of the tool's geometry. This approach makes the final data entirely independent of the size of the region initially outlined by the operator, ensuring consistent accuracy in industrial presetting.

In addition to stabilising individual 2D profiles, the aim of the software architecture developed is to ensure and quantify the repeatability of the measurement across the entire scanned volume of the tool. To achieve this, the computational pipeline incorporates a multi-profile automated processing module.

Once the operator has validated the initial positioning of the ROI and defined the error threshold on a setup profile, the software locks these spatial parameters. The system then automatically runs the `calculate_fit` algorithm on a series

of successive acquisitions, representing sequential cross-sections of the cutting edge along the Z-axis.

For each valid frame within the sequence, the algorithm independently performs the outlier rejection cycle, extracting the absolute angle and the length of the functional segment. Rather than presenting the operator with arrays of raw data, these discrete values are statistically aggregated to assess the overall consistency of the analysed geometry.

As shown in the table in the final report generated by the GUI (fig. 5.10), the software calculates and displays the key metrological indicators for both measured quantities (angle and length):

- **Mean (μ):** The arithmetic average of the results across all valid frames, representing the nominal measured value.
- **Range:** The absolute difference between the maximum and minimum recorded values within the batch, highlighting the maximum dispersion.
- **Standard Deviation (σ):** A strict quantification of the measurement repeatability and the overall stability of the automated evaluation chain.

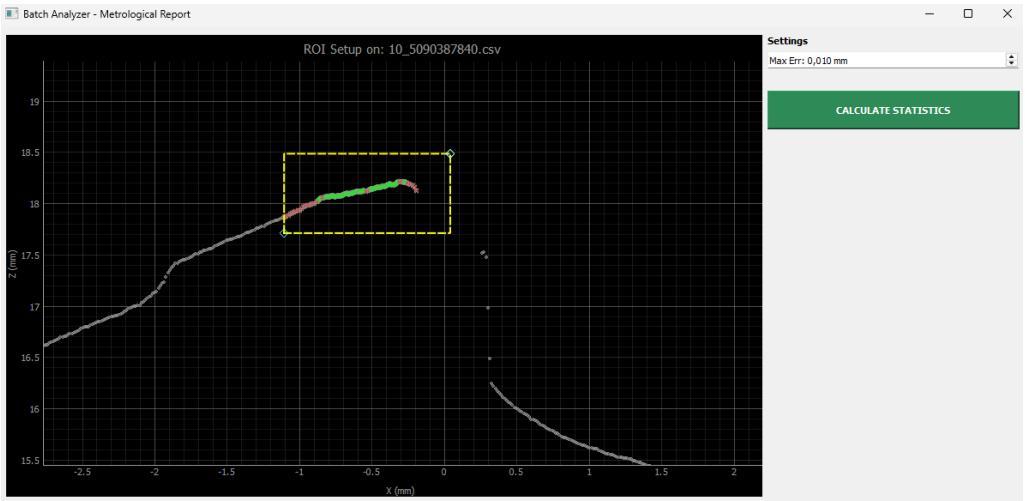

Figure 5.10: The final GUI metrological report.

5.4 Results

This section presents and discusses the experimental data obtained by applying the developed optical measurement system to a selection of significant industrial tool samples. The primary objective of this experimental campaign is twofold: first, to verify the system's accuracy in determining nominal geometric parameters (clearance/rake angles and cutting edge lengths); and second, to validate the robustness of the Iterative Robust Fitting algorithm across diverse morphological configurations.

For each sample, data was acquired following the multi-profile sequential protocol described in the previous chapter, ensuring a robust statistical baseline of 10 frames per measurement. In the following sections, the experimental results are compared against nominal design data, evaluating the mean (μ), the data dispersion (Range), and the overall system repeatability (σ) for each case study.

Feature	Mean	Min	Max	Range	σ	Threshold [mm]	Rotation [°]	Result	Expected
Ball Nose 6mm									
Rake angle [°]	24.5361	24.4167	24.6175	0.2008	0.0646	0.005	325.515	9.9489°	$6° \pm 1°$
Primary clearance [°]	22.3588	22.3391	22.3692	0.0301	0.0084	0.005	348.914	11.2728°	$14° \pm 2°$
Primary clearance [mm]	0.2811	0.2810	0.2811	0.0001	0.0000	0.005	348.914	0.2811 mm	0.3 mm
Secondary clearance [°]	39.6857	39.6804	39.6892	0.0088	0.0024	0.007	325.515	28.4006°	$30° \pm 2°$
Secondary clearance [mm]	0.7017	0.7015	0.7017	0.0002	0.0001	0.007	325.515	0.7017 mm	0.6 mm
Top Primary clearance [°]	12.3786	12.3628	12.3963	0.0335	0.0086	0.010	–	12.3786°	$14° \pm 2°$
Top Secondary clearance [°]	27.6769	27.6740	27.6790	0.0050	0.0017	0.010	–	27.6769°	$30° \pm 2°$
End Mill 6mm									
Rake angle [°]	35.2063	35.1995	35.2102	0.0107	0.0034	0.005	319.881	4.9127°	$6° \pm 2°$
Primary clearance [°]	12.2784	12.2518	12.3005	0.0488	0.0013	0.005	349.657	1.9354°	$11° \pm 2°$
Secondary clearance [°]	26.2357	26.2301	26.2459	0.0157	0.0047	0.006	352.732	18.9677°	$20° \pm 2°$
Ball Nose 12mm									
Rake angle [°]	36.7070	36.5210	36.9060	0.3850	0.1330	0.005	317.552	5.7410°	$6° \pm 1°$
Primary clearance [°]	34.1982	34.1547	34.2140	0.0593	0.0214	0.005	339.444	13.6422°	$14° \pm 2°$
Primary clearance [mm]	0.6115	0.6115	0.6116	0.0001	0.0000	0.005	339.444	0.6115 mm	0.6 mm
Secondary clearance [°]	34.8834	34.8809	34.8849	0.0040	0.0014	0.006	353.188	28.0714°	$30° \pm 2°$
Secondary clearance [mm]	1.2187	1.2187	1.2188	0.0001	0.0000	0.006	325.515	1.2187 mm	1.2 mm
Top Primary clearance [°]	13.8853	13.8838	13.8864	0.0025	0.0009	0.006	–	13.8853°	$14° \pm 2°$
Top Secondary clearance [°]	30.3410	30.3335	30.3478	0.0144	0.0060	0.005	–	30.3410°	$30° \pm 2°$

Table 5.1: Experimental results of the automated analysis across different tool geometries.

Looking at the data in the table, it is clear that the measured values for the 6 mm ball-nose cutter fall almost entirely within the tolerances specified by the manufacturer. As expected, the most critical parameter to evaluate was the rake angle, due to its extremely small size and the resulting algorithmic difficulty in accurately isolating a sufficient number of useful points on the cutting edge.

Of the tools analysed, the only two parameters found to be outside tolerance

compared with the nominal design data were the rake angle of the 6 mm ball nose and the first clearance angle of the milling cutter. To determine whether these deviations were due to a limitation of our processing system or to an actual geometric non-conformity of the samples, a joint empirical verification was carried out with Speroni's specialist technicians. Although it was not possible to obtain an absolute reference counter-value using third-party instrumentation, this qualitative analysis confirmed that the actual slope of the tool flank tends towards the measurement detected by our software, deviating from the nominal value. This result allows us to hypothesise with a high degree of certainty that the part under examination is indeed defective from a manufacturing perspective. Due to technical limitations of the investigation, it was unfortunately not possible to carry out the same verification on the rake angle.

On the contrary, the results obtained for the 12 mm ball-nose cutter fall perfectly within the manufacturing tolerances. This data highlights the accuracy of the measurement method developed, the robustness of which is likely enhanced by the larger dimensions of the workpiece. A larger effective surface area provides the Robust Fitting algorithm with a numerically larger set of data (inliers); being able to calculate the regression line over a longer segment drastically reduces statistical uncertainty, making the convergence of the measurement much more reliable and stable.

Lastly, it is essential to highlight the extremely low measurement uncertainty values (expressed as the standard deviation) recorded throughout the entire experimental campaign. This remarkable stability is a direct consequence of the extraction method adopted: averaging a set of frames that have themselves already undergone spatial averaging (from 3D to 2D) means providing the system with profiles that are intrinsically free of background noise.

Furthermore, using the spatial calculation method explained in eq. (5.4), this very low dispersion of angular values translates into an even lower uncertainty regarding segment lengths, allowing an uncertainty of length tending towards zero to be recorded in these tests.

Chapter 6

Conclusions

This thesis has led to the development and validation of an innovative optical measurement system for tool presetting, integrating advanced 3D scanning technologies within a high-precision industrial setting. The main objective, the transition from manual and subjective assessment to an autonomous and repeatable analysis process, has been fully achieved through a robust and high-performance software architecture.

The most significant technical contribution lies in the development of the Iterative Robust Fitting algorithm. This solution has proven capable of overcoming the limitations associated with operator dependency: thanks to the recursive outlier rejection logic, the system is able to isolate the actual geometric profile of the cutting edge even when starting from an initial approximate selection. The algorithm's ability to systematically converge towards valid points (inliers) ensures measurement consistency that traditional fitting methods could not guarantee on complex micro-mechanical geometries.

Experimental validation carried out on various samples has confirmed the effectiveness of the proposed approach. Of particular significance was the case study of the 6 mm end mill, where the system's accuracy enabled the identification of a geometric non-conformity compared to the nominal data, a finding subsequently confirmed by Speroni's specialist technicians. This result elevates the project from an academic prototype to a real-world quality control tool, capable of distinguishing with certainty between measurement uncertainties and manufacturing defects. Furthermore, the metrological stability achieved, with extremely low standard deviation values tending towards zero for linear measurements ($\sigma = 0$), attests to the reliability of the spatial calculation method implemented.

From an industrial impact perspective, the adoption of this technology represents a key strategic advancement for Speroni. The integration of 3D data-driven analysis makes it possible to detect and quantify critical parameters, such as rake and clearance angles on complex geometries, which were previously impossible to analyse using standard edge detection technology based solely on 2D profiles. This innovation not only expands the company's diagnostic capabilities but also ensures superior precision in tool presetting, drastically reducing setup times and margins of error in machining operations.

6.1 Future work

While the developed system has successfully validated the feasibility of 3D-to-2D optical tool presetting, several enhancements could be implemented to transition the current prototype into a fully integrated industrial solution:

- **Full Software Integration and Live Data Acquisition:** The current workflow relies on the manual export and ingestion of static CSV files. A primary future development will be the direct integration of the laser sensor's API into the Speroni software ecosystem. This would enable a live data pipeline, where the software communicates directly with the sensor, triggering scans and processing data in real-time without external procedures.
- **Automated Tool Alignment and Rotational Homing:** Currently, tool alignment and the identification of the "zero configuration" (aligning the cutting edge with the sensor's center axis) are performed manually using the sensor's native live view. This process could be fully automated by implementing an iterative rotation algorithm. By analyzing the live profile during tool rotation, the system could autonomously identify the peak of the cutting edge and command the machine's motors to lock the tool in the optimal measurement position.
- **Dynamic Exposure and Gain Control:** To ensure consistent data quality across different tool materials, an intelligent exposure algorithm should be developed. Rather than manual pixel saturation checks, the software could dynamically calculate the optimal exposure time based on the tool's reflectivity and the incident angle of the laser beam. This would eliminate measurement errors caused by over-exposure or signal loss on highly reflective surfaces.

Bibliography

[1] 3ERP, "Rake angle: Everything you need to know," 2023. https://www.3erp.com/blog/rake-angle/, Last Access 2026.02.21.

[2] TechMet Carbides, "Tool wear: Built-up edge," 2025. https://www.techmet-carbide.com/blog/133/tool-wear-built-up-edge, Last Access 2026.02.24.

[3] J. Lee, C. L. Chavez, and J. Park, "Parameters affecting mechanical and thermal responses in bone drilling: A review," *Journal of Biomechanics*, vol. 71, pp. 4–21, 2018.

[4] Baer Tools, "Geometria degli utensili: l'importanza dell'angolo di spoglia e di petto," 2023. https://baer.tools/it/blog/detail/01903058e2047ec8a1a1510cf9493fa3, Last Access 2026.02.21.

[5] M. A. H. Mithu, "Machine tools & machining (ipe 441): Theory of metal cutting," 2023. https://it.scribd.com/document/652409407/Metal-Cutting, Last Access 2026.02.24.

[6] Tonzamaking, "What effect does the geometry angle of a cutting tool have on cutting?," 2024. https://tonzamaking.com/blog/what-effect-does-the-geometry-angle-of-a-turning-tool-have-on-cutting/, Last Access 2026.02.21.

[7] Speroni S.p.A., "Stp futura - tool presetting and measuring systems," 2024. https://speroni.info/en/prodotti/stp-futura/, Last Access 2026.03.14.

[8] LMI Technologies, "Case study: Zoller integrates 3d scanners for sub-micron tool inspection," 2016. https://lmi3d.com/wp-content/uploads/2016-08/CS_ZOLLER_US_WEB.pdf, Last Access 2026.03.15.

[9] Bruker Alicona, "Advanced focus variation technology for 3d metrology," 2025. https://www.alicona.com/it/tecnologie, Last Access 2026.03.15.

[10] Xpert3D, "Alicona infinitefocus sl: Optical 3d micro coordinate measurement system," 2021. https://xpert3d.ca/alicona/alicona-infinitefocus-sl/, Last Access 2026.03.15.

[11] Carl Zeiss Industrielle Messtechnik, "Optical metrology: The principle of laser triangulation," 2024. https://www.zeiss.it/metrologia/esplora/argomenti/triangolazione.html, Last Access 2026.02.27.

[12] Kreon Technologies, "How does laser triangulation 3d scanning technology improve manufacturing processes?," 2024. https://www.kreon3d.com/it/article/how-does-laser-triangulation-3d-scanning-technology-improve-manufacturing-processes, Last Access 2026.02.27.

[13] Novus Light Technologies Today, "Pros and cons of popular 3d technologies," 2019. https://www.novuslight.com/pros-and-cons-of-popular-3d-technologies_N8910.html, Last Access 2026.02.28.

[14] M. Zaiß, J. Demmerle, J. N. Oergele, and G. Lanza, "New concepts for quality assurance of lightweight material," *Procedia CIRP*, vol. 66, pp. 259–264, 12 2017.

[15] LMI Technologies, "Official website and three dimensional sensor specifications," 2025. https://lmi3d.com/, Last Access 2026.03.23.

[16] Teledyne Vision Solutions, "Official website and profiler specifications," 2025. https://www.teledynevisionsolutions.com/, Last Access 2026.03.23.

[17] Automation Technology, "At sensors official website and technical datasheets," 2024. https://www.at-sensors.com/, Last Access 2026.03.23.

[18] Artec 3D, "Structured light three dimensional scanning: How it works," 2022. https://www.artec3d.com/learning-center/structured-light-3d-scanning, Last Access 2026.03.01.

[19] J. Geng, "Structured-light 3d surface imaging: a tutorial," *Adv. Opt. Photon.*, vol. 3, pp. 128–160, Jun 2011.

[20] VA Imaging, "Tecnologia a luce strutturata." https://va-imaging.com/it/blogs/machine-vision-knowledge-center/tecnologia-luce-strutturata, Last Access 2026.03.01.

[21] e-con Systems, "What is a stereo vision camera," 2023. https://www.e-consystems.com/blog/camera/technology/what-is-a-stereo-vision-camera-2/, Last Access 2026.03.04.

[22] LearnOpenCV, "Introduction to epipolar geometry and stereo vision," 2020. https://learnopencv.com/introduction-to-epipolar-geometry-and-stereo-vision/, Last Access 2026.03.04.

[23] Baeldung, "Disparity map in stereo vision," 2023. https://www.baeldung.com/cs/disparity-map-stereo-vision, Last Access 2026.03.06.

[24] Luxonis, "Stereo depth formula and configuration," 2024. https://docs.luxonis.com/hardware/platform/depth/configuring-stereo-depth, Last Access 2026.03.06.

[25] IDS Imaging Development Systems, "Industrial cameras and machine vision," 2026. https://en.ids-imaging.com/, Last Access 2026.03.23.

[26] Edmund Optics, "Depth of field and depth of focus," 2021. https://www.edmundoptics.com/knowledge-center/application-notes/imaging/depth-of-field-and-depth-of-focus/, Last Access 2026.03.07.

[27] S. Nayar and Y. Nakagawa, "Shape from focus," *IEEE Transactions on Pattern Analysis and Machine Intelligence*, vol. 16, no. 8, pp. 824–831, 1994.

[28] iMAGE S S.p.A., "Sistemi 3d e panoramica tecnologica," 2025. https://www.imagesspa.it/sistemi-3d, Last Access 2026.03.09.

[29] Alfatest S.r.l., "Microscopia a super-risoluzione," 2024. https://www.alfatestbio.it/tecniche/microscopia-super-risoluzione/, Last Access 2026.03.09.

[30] GVDA Instrument, "How confocal microscopy produces three dimensional images," 2024. https://it.gvda-instrument.com/info/how-confocal-microscopy-produces-three-dimensi-101366559.html, Last Access 2026.03.10.

[31] Bruker Corporation, "Comparing 3d optical microscopy techniques for metrology applications," 2013. https://www.bruker.com/en/prod

ucts-and-solutions/test-and-measurement/3d-optical-profilers/resource-library/an-503-comparing-3d-optical-microscopy-techniques-for-metrology-applications.html, Last Access 2026.03.10.

[32] Chans Machining, "Precision vs. accuracy: What's the difference?," 2023. https://chansmachining.com/precision-vs-accuracy/, Last Access 2026.03.26.

[33] P. Bhandari, "Random vs. Systematic Error: Definition & Examples," 2023. https://www.scribbr.com/methodology/random-vs-systematic-error/, Last Access 2026.03.26.

[34] S. A. Mondal, "Understanding MAE, MSE, and RMSE: Key Metrics in Machine Learning," 2024. https://dev.to/mondal_sabbha/understanding-mae-mse-and-rmse-key-metrics-in-machine-learning-4la2, Last Access 2026.03.28.

[35] JMP Statistical Software, "Standard Deviation: Definition, Formula and Example," 2021. https://www.jmp.com/it/statistics-knowledge-portal/measures-of-central-tendency-and-variability/standard-deviation, Last Access 2026.03.28.

[36] NumPy Developers, *NumPy Reference: numpy.polyfit*, 2025. https://numpy.org/doc/stable/reference/generated/numpy.polyfit.html, Last Access 2026.03.25.

[37] S. M. Ross, *Introduction to Probability and Statistics for Engineers and Scientists*. Academic Press, 5th ed., 2014.

[38] Euresys, *Open eVision User Guide: Laser Line Extraction*, 2024. https://documentation.euresys.com/Products/Open_eVision/Open_eVision/en-us/Content/03_Using/6_3D_Processing/3_Easy3DLaserLine/Laser_Line_Extraction.htm, Last Access 2026.03.30.

Appendix A

Codes

Listing A.1: Iterative Robust Fitting algorithm.

```
def calculate_fit(self, x_arr, z_arr, x_min, x_max, z_min, z_max, threshold):

    # 1. Isolate points strictly within the bounding box
    mask = (x_arr >= x_min) & (x_arr <= x_max) & (z_arr >= z_min) & (z_arr <= z_max)
    x_work, z_work = x_arr[mask].copy(), z_arr[mask].copy()

    if len(x_work) < 3: return None
    m, q, valid = 0, 0, False

    # 2. Iterative Robust Regression Loop
    for _ in range(200):
        if len(x_work) < 3: break

        # Standard linear regression on current inliers
        m, q = np.polyfit(x_work, z_work, 1)

        # Calculate Euclidean (perpendicular) distance for outlier detection
        dists = np.abs(m * x_work - z_work + q) / np.sqrt(m**2 + 1)
        max_d, idx_max = np.max(dists), np.argmax(dists)

        if max_d <= threshold:
            valid = True
            break
```

```
        else:
            # Remove the point with the highest residual
            x_work = np.delete(x_work, idx_max)
            z_work = np.delete(z_work, idx_max)

    if not valid: return None

    # 3. Geometric parameters evaluation
    angle = np.degrees(np.arctan(m))
    idx_min, idx_max = np.argmin(x_work), np.argmax(x_work)
    length = np.hypot(x_work[idx_max] - x_work[idx_min], z_work[
    idx_max] - z_work[idx_min])

    return {'angle': angle, 'length': length, 'm': m, 'q': q}
```